# Manipulation of electronic band structure by doping colloidal gallium oxide nanocrystals and its impact on photocatalysis

by

Susi Jin

A thesis

presented to the University of Waterloo

in fulfillment of the

thesis requirement for the degree of

Master of Science

in

Chemistry

Waterloo, Ontario, Canada, 2018

## Author's Declaration

I hereby declare that I am the sole author of this thesis. This is a true copy of the thesis, including any required final revisions, as accepted by my examiners. I understand that my thesis may be made electronically available to the public.

## Abstract

Semiconductor photocatalyst have been of interest due to its robust nature, non-selectivity, low toxicity, and high tunability. Its various applications such as water splitting, water purification, anti-microbial, etc make this a desirable class of material to explore. However, there are defects in semiconductors that may impact the rate of photocatalysis. This study aims to illuminate the role of defects in photocatalysis.

For this study, the defect nature of γ- $Ga_2O_3$ was manipulated by doping the crystal structure with indium acetylacetonate ($In(acac)_3$) or zinc nitrate ($Zn(NO_3)_2$) during colloidal synthesis in oleylamine. The electronic structure was analyzed to determine the correlation with photocatalysis using rhodamine-590 (Rh-590) as a model reactant. These results demonstrate that dopants would decrease the wide band gap of γ- $Ga_2O_3$ but maintain the defect spinel structure up to 15%. However, different dopants impact defects differently, which was reflected in photoluminescence (PL) emission spectra and the fast regime in time-resolved PL measurements. PL emission was derived from the recombination of the donor and acceptor pairs (DAP). Doping with $In^{3+}$ has a maximum PL red shift of 24 nm, while doping with $Zn^{2+}$ has a maximum PL red shift of 9 nm. This red shift indicates an increase in DAP distance and/or a decrease in defect concentration. Time resolved PL measurements using a TCSPC method with a 200 ns measurement range demonstrates that doping with 15% indium would decrease the average lifetime (LT) from 11.0 ± 0.3 ns to 3.4 ± 0.4 ns, while doping with 15% zinc

would increase the LT to 15.1 ± 0.4 ns. Therefore, there was a positive correlation between the average LT and the rate constant derived from photocatalysis with a critical value ca. 8 ns where the apparent rate constant was not impacted from further increasing LT.

In conclusion, there is a potential to manipulate the electronic structure using dopants to impact photocatalysis. In addition, synthesis of $Ga_{2-x}M_xO_3$ ($M=In^{3+}$ or $Zn^{2+}$) was successfully synthesized using a colloidal synthesis method. A relationship can also be developed between the average LT calculated from time-resolved PL and the apparent rate constant from the photocatalytic degradation of a model reactant.

## Acknowledgments

First, I would like to thank my supervisor, Dr. Pavle V. Radovanovic, for his passion and wealth of knowledge. I am extremely appreciative for his guidance and encouragement through the challenges I faced throughout my degree. I would also like to thank my committee members, Dr. Frank Gu and Dr. Eric Prouzet for their assistance in my graduate studies.

My degree would not have been completed without the help from many people. I would like to extend my gratitude to Dr. Carmen Andrei at the Brockhouse Institute for Materials Research at McMaster University for her assistance in TEM image collection. I would also like to acknowledge the Klinke group at the University of Waterloo for their help and guidance with XRD collection. I would also like to thank Andrew Kacheff from the Prouzet group at the University of Waterloo for his assistance in BET surface measurements and for being so accommodating. I would also like to acknowledge Dr. Jonathan Baugh and Dr. Howard Siu for being great mentors during teaching assistantships.

I would also like to thank the past and present group members at the Radovanovic group for their constant encouragement and advice. Specifically, I would like to thank Vahid for always being available to help along my way especially during the early stages of my degree. In addition, I would like to extend my gratitude to Dr.

Joshua Byers for his help with this project. I would also like to thank Manu for his assistance with obtaining EDX data on the SEM and for editing a portion of my thesis. In addition, I would like to thank Natalie Garnet for taking the time to read and revise my thesis. Lastly, I would also like to acknowledge Paul for his assistance with TCSPC (HORIBA) measurements.

Lastly, I would like to thank my friends, family, and significant other. I am thankful for your constant support and encouragement to achieve my goals. Everyone was a fundamental part of my success in obtaining this degree.

## Table of Contents

## List of Figures

## List of Tables

## List of Abbreviations

| | |
|---|---|
| A.U. | Arbitrary Units |
| BET | Brunauer–Emmett–Teller |
| BG | Band Gap |
| ca. | circa |
| CB | Conduction Band |
| DAP | Donor-Acceptor Pair |
| $e^-$ | Electron |
| EDX | Energy-dispersive |
| Ea | Energy of acceptor |
| Ebg | Energy of band gap |
| Ec | Energy of Coulombic interaction |
| Ed | Energy of donor |
| $h^+$ | Hole |
| HRTEM | High resolution TEM |
| ITO | Indium Tin Oxide |
| $k_{app}$ | Apparent rate constant |
| LT | Lifetime |
| NC | Nanocrystal |

| | |
|---|---|
| nm | nanometer |
| ns | Nanosecond |
| PL | Photoluminescence |
| REDOX | Reduction oxidization |
| Rh-590 | Rhodamine-590 |
| SC | Semiconductor |
| SEM | Scanning electron microscopy |
| TCO | Transparent conducting oxide |
| TCSPC | Time correlated single photon counting |
| TEM | Transmission electron microscopy |
| μs | Microsecond |
| UV-Vis | Ultra-violet visible |
| VB | Valence band |
| XRD | x-ray diffraction |

# Chapter 1.0: Introduction

## 1.1: Introduction to Semiconductors and Transparent Conducting Oxides

A semiconductor is a class of material that exhibits partial conductive properties, between that of a metal with high conductivity, and insulator with no conductivity.[1,2] This arises from the separation of energy levels situated between >0eV to <5eV. Due to its unique properties, it is an essential component for electronic circuits.

Semiconductor materials can be intrinsic or extrinsic as shown in Figure 1.1. Typically intrinsic semiconductors are pure semiconductors with no dopant/impurity while extrinsic semiconductors are doped and exhibit p- or n-type characteristics.[1] When the semiconductor is doped with an element that has more valence electron(s) than its host, it would produce an n-type semiconductor.[1] The conduction band (CB) would be partially filled, and considered to be negatively charged with an increase in donors.[1] Conversely, p-type semiconductors are doped with an element with less valence electron(s) than its host, producing holes in the lattice. Thus, the valence band (VB) would be partially empty and considered positively charged with an increase in acceptors. Due to the holes or electron in n- or p-type semiconductors respectively, the electrons or holes can have greater mobility, increasing conductivity.

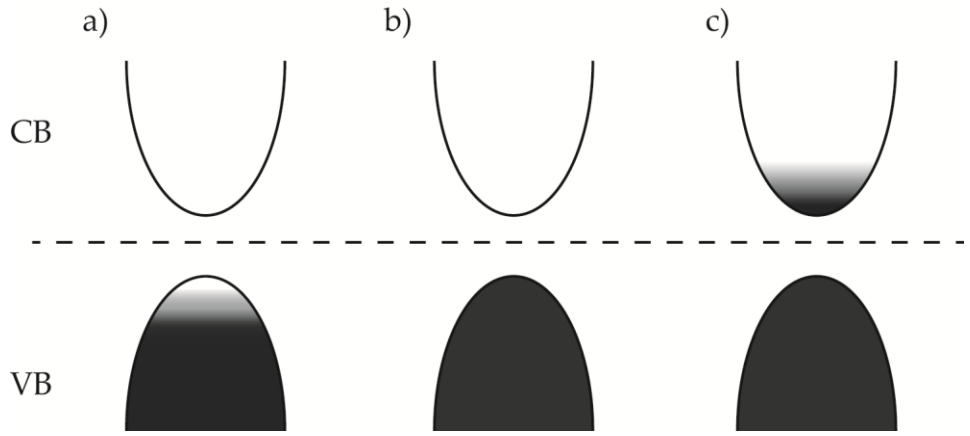


**Figure 1.1: Energy level occupation of a) p- , b) intrinsic, and c) n-type semiconductors. Black indicated filled energy levels and white indicate unfilled.**

Another type of semiconductor generating interest are those with a wide band gap (>3eV), enabling transparency in the visible region.[3–5] These are called transparent conducting oxides (TCO) and display quantum and classical phenomena.[3] These materials are valuable due to the ability to manipulate the conductivity, high stability, and absorption in the infrared region. The most commonly known TCO is indium tin oxide (ITO) used in electronic displays, photovoltaics, smart windows, etc.[4] Conductivity can be manipulated by modifying the concentration of tin in the indium oxide lattice. An increase in conductivity however, would decrease the transparency which may hinder some applications. Majority of naturally occurring TCOs are n-type semiconductors.

## 1.2: Photocatalysis

Photocatalysis is defined as the harness of light to speed up or activate a given reaction.[6] This can be viewed as a type of artificial photosynthesis. It is often used for organic compound removal (phenols, dyes, toluene, pharmaceuticals, bacteria, etc), sterilization, heat transfer/dissipation, or water splitting.[6–11] This is often implemented as a heterogeneous photocatalysis as homogenous photocatalysis imposes the issue of catalyst removal. The most common heterogeneous photocatalyst are semiconductors due to low toxicity, recyclability, low cost, and tunability. [12] This is classified as a type of advance oxidation process (AOP). For efficient photocatalysis, 5 processes must occur; 1) diffusion from solution to surface of the catalyst, 2) adsorption to surface of the catalyst, 3) reaction on surface of the catalyst, 4) desorption on surface of catalyst, and 5) diffusion away from surface of the catalyst. [13]

If one of those processes does not occur, efficient photocatalysis would fail. The reaction for process 3) undergoes a redox reaction from the photogenerated electrons and holes. Generation of the electrons and holes occurs upon absorption of a photon with an energy equal to or greater than the band gap of the semiconductor, an electron can be excited into the conduction band while leaving a hole in the valence band.[6,7,14] Following that, the photogenerated electrons would reduce surface bound ligands, such as oxygen to produce superoxide radicals (eq 1).[6,7,13] The holes would oxidize surface

bound ligands, such as water to produce hydroxyl radicals (eq 2).[7] These radicals can then react with other adsorbed species to degrade them and/or produce more radicals (eq 4).

$$e^- + O_2 \rightarrow \cdot O_2^- \quad (1)$$

$$h^+ + OH^- \rightarrow \cdot OH \quad (2)$$

$$h^+ + H_2O \rightarrow \cdot OH + H^+ \quad (3)$$

$$\cdot OH + org \rightarrow H_2O + \cdot Org \rightarrow CO_2 + H_2O + \cdots \quad (4)$$

Fujishima et al. (2008) states for efficient photocatalysis, oxidation and reduction must occur at similar rates to be considered a catalyst.[6] If it were not balanced, the catalyst would be quenched where recovery of the catalyst would not occur and thus cannot be used for multiple cycles rendering it nil.[6] However, some scavenger studies have been conducted that demonstrates this may not always be the case as some species are more favourable than others for photocatalysis. Further studies need to be conducted to properly understand the process.

The photogenerated electrons and/or holes may also reduce and/or oxidize the surface bound species depending on the redox potential of the surface bound species relative to the location of the VB and CB of the semiconductor and the binding strength

on the surface.[7] In other words, the optical band gap of the semiconductor must encompass the redox potentials for redox to occur.[15]

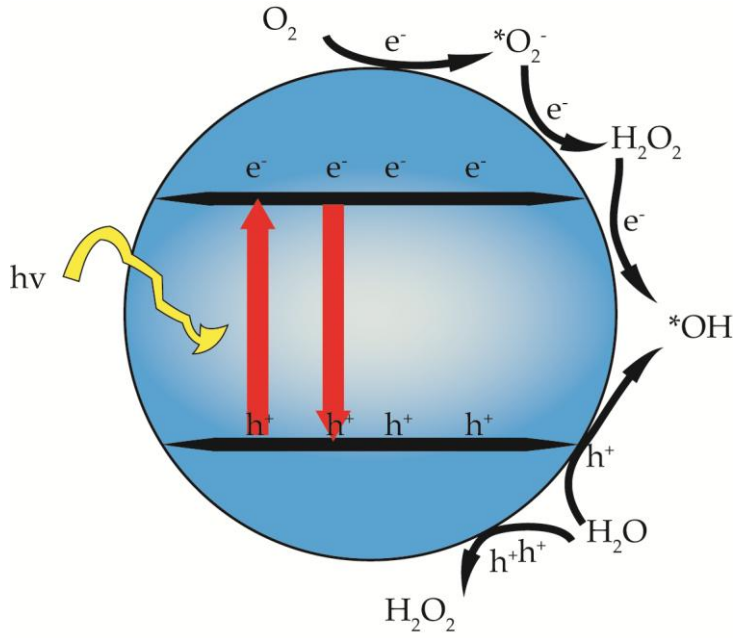


**Figure 1.2: REDOX reactions on surface of catalyst during exposure to light.**

Currently, there has been research conducted on semiconductors such as $TiO_2$, ZnO, $Fe_2O_3$, CdS and $SnO_2$ for photocatalysis. These materials are environmentally benign, stable, and have high activity. These materials are also non-selective towards the reactive species, thus making it an eligible option for water treatment.[15] Currently, $TiO_2$ has been studied extensively; however $TiO_2$ is only able to degrade low to medium concentrations of contaminants because of its low efficiency and limited flux.[6] Therefore other materials have been studied to determine the mechanism and methods to increase efficiency.

Efficiency of photocatalysis can fail by having a modest surface area.[16] Lower surface area indicates a lower concentration of binding sites on the surface. Therefore, more surface area indicates more binding site, and a higher rate of photocatalyis. Recombination of electrons and holes is another way the efficiency of photocatalysis can be reduced. The electrons and holes may recombine thus reducing the probability of interfacial charge transfer for photocatalysis. Thus, recombination is a competing process for photocatalysis. For efficient photocatalysis, the rate of recombination needs to be mitigated to favour photocatalysis. Efficient charge separation distance may diminish recombination and thus improve photocatalysis. Charge separation can be implemented in a variety of ways such as introduction of a phase junction.[13] This can either be a heterojunction or homojunction. There are three different types of junctions that can be formed, type I, type II, and type III illustrated in Figure 1.3.[17] Typically, type II band alignment is favoured as one phase would facilitate electrons, while the other for holes providing sufficient charge separation.[18] However, type I may be adequate as some studies found formation of a type I junction increased activity versus the catalyst alone.[19] Moreover, type III may not provide charge separation since it may not efficiently facilitate separation of the charges since the band alignment may not allow this. Furthermore, defects may impact interfacial charge r transfer. One such theory indicates that deep defects would aid recombination, while surface defects would aid photocatalysis.[15,20–22] Deep defects would act as recombination centres, thus reducing

photoctalysis. However, surface defects act as traps for interfacial charge transfer to reactive species. Therefore, surface defects should be maximized, while deep defects should be minimized. However, a lot of defect structure is not well understood for photocatalysis.

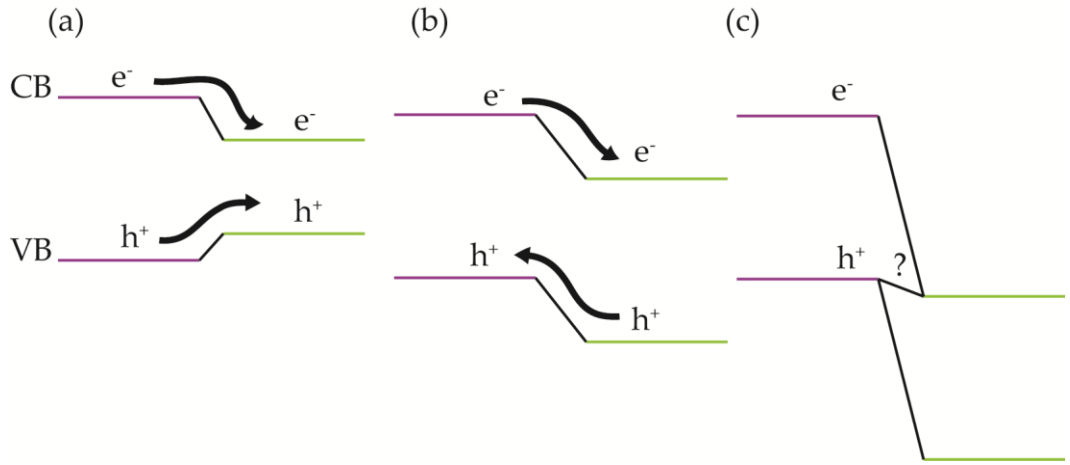


**Figure 1.3: Different band alignments of phase junctions. Different colours denote different band structures. Arrows demonstrate the direction of electron and hole movement. A) Type I, (b) type II, (c) type III.**

## 1.3: $Ga_2O_3$

Gallium oxide is a group IIIA TCO that has been generating interest due to its high stability, and defective lattice. This material is a natural n-type semiconductor with 5 known polymorphs (α, β, γ, δ, and ε) and a wide band gap (~4.9eV).[23] The most stable polymorph is the β-phase which has a monoclinic crystal structure shown in Figure 1.4(a). When all other polymorphs are heat treated to a critical temperature, the lattice would transform to the β-phase.[24] Of particular interest is γ-phase $Ga_2O_3$ with the

crystal structure shown in Figure 1.4(b). This phase consist of a defect spinel structure, similar to γ-$Al_2O_3$, and contains oxygen vacancies and gallium-oxygen vacancies. In this structure, gallium can occupy both the tetrahedral site and the octahedral site. Since the band gap is large, the photoadsorption range is limited to the UV-region of the electromagnetic spectrum. However, depending on the application this may be a desirable trait as it would be transparent in the visible region.

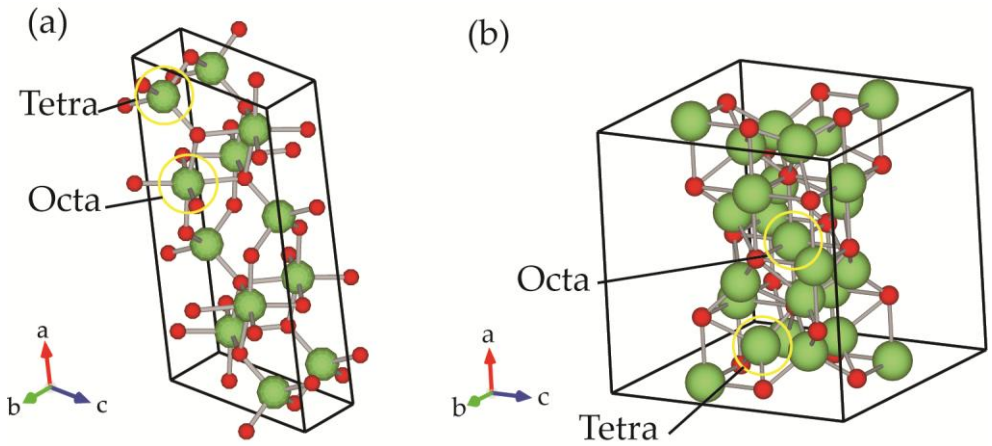


**Figure 1.4: Crystal structure of $Ga_2O_3$ (a) β-phase (b) γ -phase. Green spheres represent gallium ions and red spheres represent oxygen ions. Circled are the two different coordinations.**

There is limited data pertaining to $Ga_2O_3$ and its photocatalytic ability in literature. One such paper, Wang et al. (2012), observed the activity of $\alpha$-β phase junction for water splitting.[25] They concluded that a phase junction improves photocatalytic ability over the individual polymorphs. However, when Jin et al. (2015)

analyzed γ-β phase junction for water splitting, they observed the opposite trend when a junction was formed.[26] Instead of improving their activity, the phase junction decreased their activity relative to the individual polymorphs, a 10% and 90% decrease in activity relative to β- and γ-phase respectively.[26] In addition, they discovered that the γ-phase had a lower activity than the β-phase. The reasoning can be attributed to higher crystallinity of the α-β phase junction compared to the γ-β enabling efficient charge separation.[26] Therefore, the low activity can be attributed to lower crystallinity, and these defects can act as recombination centres. Furthermore, the band alignment was type I for the γ-β while it was type II for α-β further improving charge separation. However, the conclusion may not be that simple since there are controversial data present. A study done by Ghodsi et al (2017) on γ-$Ga_2O_3$ indicates that γ-phase has a greater activity than β-phase.[24] This can be attributed to the electronic structure, location and concentration of defects that can modify the degradation rate that Wang et al. (2012) and Jin et al. (2015) had not considered. Therefore, there is limited information about the role of defects on the rate of photocatalysis for a broad range of systems. To further explore the effect of defects on photocatalysis, the host system can be doped with metal ion(s).

## 1.4: $In_2O_3$

Indium oxide is a group IIIA TCO with a band gap of ~3.0 eV and consists of two different crystal structures, cubic and metastable rhombohedral with octahedral

coordination shown in Figure 1.5.[27] For the colloidal synthesis method, rhombohedral has a corundum structure, and exists at low synthesis temperatures while cubic indium oxide has a bixbyite type structure and can exist at high temperatures.[28]

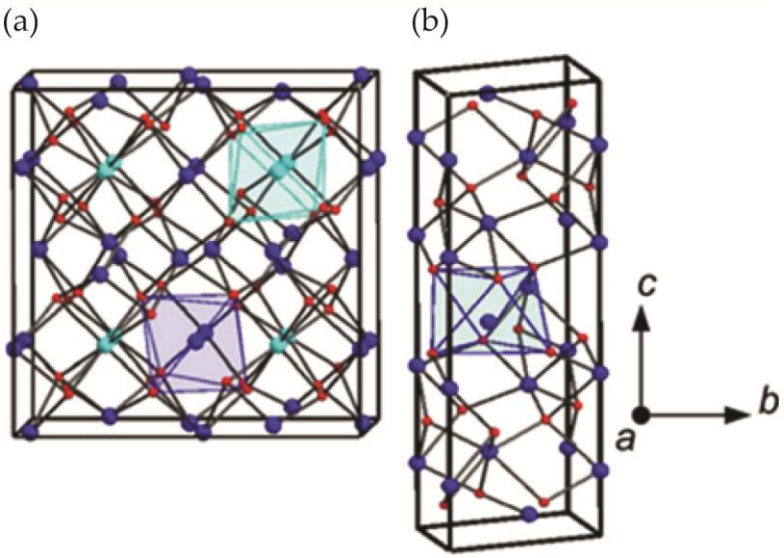


**Figure 1.5: Crystal structure of $In_2O_3$. [29] (a) cubic (b) rhombohedral. Light blue spheres represent indium with a octahedral coordination. Dark blue represent indium with a trigonal prismatic coordination. Red spheres represent oxygen.**

Indium oxide does not exhibit any significant photocatalysis from previous studies. It is believed that this can be attributed to the location of the band gap with respect to the redox potentials of hydroxyl radical formation.[30] The conduction band of $In_2O_3$ is below the reduction potential for hydrogen, thus only oxidation would occur resulting in an excess of photogenerated electrons.[31] Therefore, photocatalysis will not occur unless the CB minimum is increased to ensure reduction is occurring. This can be

done by doping, such as with tin to produce indium tin oxide (ITO). For example, Kumar et al (2011) produced ITO films with a band gap ca. 3.5 eV for photocatalysis.[32] This band gap is greater than $In_2O_3$, and will absorb at lower wavelengths. Kumar et al (2011) demonstrated that there was rate constant of 0.000192 $min^{-1}$ for commercial ITO, and a maximum of 0.0006 $min^{-1}$ for the thin films towards degradation of rhodamine-B dye when exposed to 254 nm light.[32] Therefore, they were able to demonstrate photocatalytic activity by manipulating the band gap.

## 1.5: ZnO

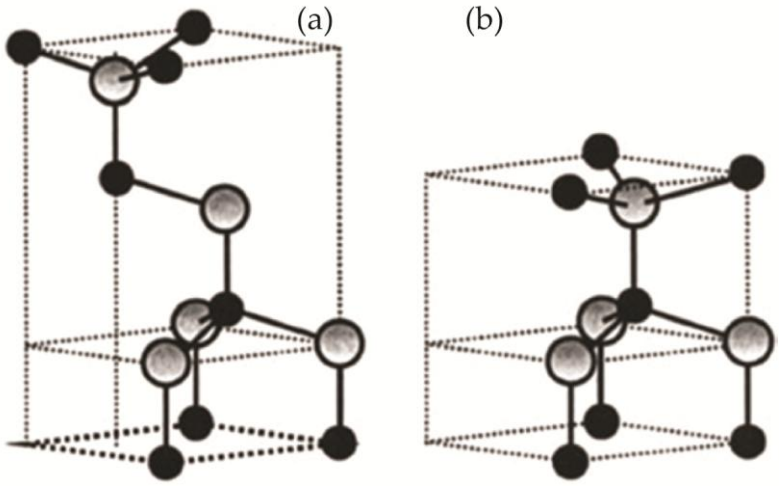


**Figure 1.6: Crystal structure of zinc oxide with (a) zinc blende (b) wurtzite. Black spheres represent oxygen. Grey spheres represent zinc.** [8]

Zinc oxide is a group IIB n-type TCO with a direct band gap of ~3.3 eV.[33–35] It has the wurtzite or zinc blende crystal structure with tetrahedral coordination shown in

Figure 1.6.[8,33] This material has been studied extensively for photocatalysis with promising results.

For example, Daneshvar (2004) reviewed ZnO as an alternative to $TiO_2$.[36] In this study, they used acid red 14 as the model reactant and determine the rate constant to be 0.0548 $min^{-1}$.[36] There is also the ability to tune the light absorption of the material to the visible region. This is favourable as majority of the solar energy is in the visible region. Tuning of the absorption can be done by modifying the band gap towards lower energies. Another method is to create a junction, where a certain species can absorb in the visible region. This would also produce efficient charge separation. For example, Wang et al (2017) looked at ZnO-SnS p-n junctions for photocatalysis.[19] They observe a 10 times increase in photocatalytic activity from pure ZnO and 2 times greater than SnS with a formation of a junction.[19] They attribute this increase in activity towards efficient charge separation towards the type I band alignment of the heterojunction.[19] Another method similar to phase junction is to have surface complexes that will absorb in the visible region and transfer energy to the ZnO. This species will not undergo photoexcitation, which means that it does not have to be a semiconductor.[37] Therefore, polymers, dyes, metals, cocatalysts, etc, can be fixed on the surface to act as visible light absorbers.[30,37,38] This broadens the scope of the material, but has its limitations.

## 1.6: Doping Semiconductors

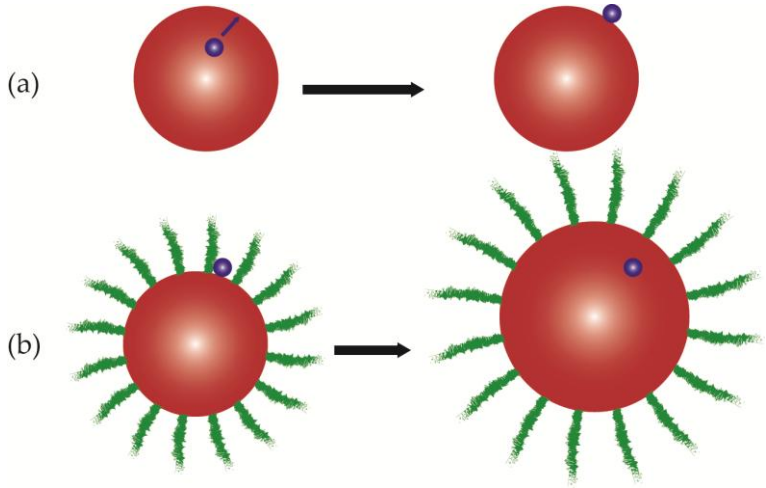


**Figure 1.7: Demonstration of different mechanisms that occur during doping. A) self-purification of the dopant (blue sphere) from the bulk (red sphere). B) Trapping of the dopant (blue sphere) using surfactants (green lines) incorporated into the bulk (red sphere).**

Doping semiconductors can influence magnetic, luminescent, physical, optical, and/or electronic properties.[39,40] These properties can be tailored for various applications such as lasers, bioimaging, optical gain devices, electroluminescence devices, solar cells, etc. Resulting doping can produce n- or p- type semiconductors as previously discussed. Often colloidal synthesis of doped semiconductors optimizes dopant incorporation. However, there are thermodynamic and kinetic factors that affect efficiency of dopant incorporation during nucleation.

First, the thermodynamic factors would impact the efficiency of doping through diffusion of the dopant to the surface demonstrated in Figure 1.7(a).[40,41] This occurs

through a self-purification mechanism where the dopant is expelled to the surface and Gibb's free energy is minimized. However, this often occurs at high temperatures, such as 1000 °C, while a majority of colloidal synthesis occurs at 350 °C or less. In addition, this is based off the assumption that the nanocrystals (NC) and the surrounding environment is in thermodynamic equilibrium.

Secondly, kinetics factors would impact doping by varying activation barriers if there is no thermodynamic equilibrium. The dopant must initially remain trapped on the surface to prevent diffusion and bulk material will surround the dopant to incorporate the dopant into the structure. For example, surfactants may trap the dopants and be incorporated during nucleation without self-purification as shown in Figure 1.7 (b).

Efficient incorporation of a dopant would mitigate self-purification and ensure that dopants would become incorporated during nucleation. Doping metal and transition metals into semiconductors would impact the band structure. Typically, doping of semiconductors can produce n- or p-type as previously discussed, where n-type may induce a donor band below the CB minimum while p-type may increase acceptor bands above the VB maximum. However, new band structures may be formed that are not within the band gap.[15,42–44] Furthermore, doping may also impact the optical band gap. The band gap would be modified depending on the location of the CB and

VB of the two oxides.[15,31] For instance, if a TCO with a large band gap were to be doped with a TCO with a smaller band gap then the band gap of the alloy would be an average of the two. Therefore, formation of new band structures and/or modification of band gap would occur during doping.

## 1.7: Motivations and Scope of the Thesis

$\gamma$- $Ga_2O_3$ makes an excellent model system to manipulate and study the impact of defects on photocatalysis since this structure has a high concentration of defects, stability, effective redox potential from the wide band gap, and high photocatalytic ability. This study could give better insight on factors that may impact photocatalysis and how to monitor the differences.

For this project, the focus was to determine the relationships between defects and electronic band structure to the apparent rate constant of photocatalysis. $\gamma$ - $Ga_2O_3$ was doped with $In^{3+}$ or $Zn^{2+}$ to modify the band structure using a known colloidal synthesis method. Different doping ion concentrations were used where the crystal structure remains defect spinel. The product was annealed to remove any surface bound ligands, and analyzed using x-ray diffraction patterns to monitor the crystal structure. The band structure would be monitored using UV-Vis absorption and PL emission. Time-resolved PL was also impacted, either shortening or lengthening the lifetime depending on the dopant. Lastly, photocatalytic degradation using rhodamine-590 (Rh-590) as the

model reactant was also done on all samples to correlate the photocatalysis to the band structure and defects.

Ultimately, utilizing $\gamma$-$Ga_2O_3$ as a model system, a relationship between PL or time-resolved PL and relative efficiency of photocatalysis may be established. In addition, this study may highlight the relationships between defects and photocatalysis for this system. Lastly, doping may be a method to engineer varying lifetimes and apparent rate constant for photocatalysis.

# Chapter 2.0: Experimental methods

## 2.1: Materials

All materials were used as is by the manufacturer. No further purification was performed. Indium acetylacetonate ($In(acac)_3$, 98%), gallium acetylacetonate ($Ga(acac)_3$, 98%) was purchased from STREM Chemicals. Oleylamine (70%) and zinc nitrate hexahydrate ($Zn(NO_3)_2*6H_2O$, 98%) was purchased from Sigma Aldrich. Methanol (99%) was purchased from Fisher scientific.

## 2.2: Synthesis

### *2.2.1: Synthesis of $Ga_2O_3$*

Synthesis of $\gamma$-$Ga_2O_3$ has been previously reported and followed with small modifications.[23] 2 g of $Ga(acetylacetonate)_3$ and 20 mL of oleylamine is combined in a 100 mL round bottom flask. The flask was fitted with a condenser, and heated to the desired synthesis temperature under an argon atmosphere. Once the desired temperature was reach, the solution remained at that temperature for 1 hour. After the hour, the flask was cooled to room temperature for further purification. Once cooled, the solution was precipitated with methanol and centrifuged to retrieve the pellet. The precipitate was rinsed 3 more times with methanol to remove any surface bound oleylamine. A small amount of the NC was dissolved in hexane for UV-Vis absorption measurements, while the remaining aliquot was dried overnight on a watch glass. The

dried sample was then ground into a powder, and annealed in a preheated furnace (Vulcan A-130) at 400 °C for 2 hours.

### *2.2.2: Synthesis of Indium or Zinc doped $Ga_2O_3$*

Synthesis of doped $Ga_2O_3$ has been previously reported for indium, these methods were followed with some modifications with indium or zinc as the dopant.[45] Doped $Ga_2O_3$ was synthesized by stochiometric additions of In(acetylacetonate)$_3$ or $Zn(NO_3)_2 6H_2O$ with 2g of Ga(acetylacetonate)$_3$ in a 100 mL three neck round bottom flask. 20 g of oleylamine was added as solvent and the flask was fitted with a condenser. The flask was heated to the desired synthesis temperature under a flow of argon while stirred with a magnetic stir bar. Once the desired synthesis temperature was reached, the flask remained at that temperature for 1 hour. After that hour, the flask was cooled to room temperature. Once cooled, the particles were precipitated with methanol and centrifuged to collect the pellet. The precipitate was further rinsed with methanol three more times. A small portion of the particles were dispersed in hexane for UV-Vis absorption measurement and the remaining portion was dried using acetone overnight in a watch glass. The dried sample was then annealed in a preheated furnace (Vulcan A-130) at 400 °C for 2 hours.

## 2.3: Characterization

### *2.3.1: XRD*

X-ray diffraction (XRD) was collected for all powder samples on an INEL powder diffractometer equipped with a position-sensitive detector using a monochrome Cu-K$\alpha$ radiation ($\lambda$ = 1.540598 Å). Each sample was ground into a fine powder, and collected on an aluminum sample holder for 10 mins. This instrument belongs to Dr. Holger Kleinke from the University of Waterloo.

### *2.3.2: UV-Vis abs*

UV-Vis absorption spectra were done on a Varian Cary 5000 UV-vis-NIR spectrophotometer at room temperature with data collected from 200-800 nm. Samples were prepared in hexane as previously outline in synthesis methods.

### *2.3.3: Transmission Electron Microscopy (TEM)*

Transmission electron microscopy (TEM) imaging were done on a JOEL-2010F microscope operating at 200 kV from the Canadian centre for Electron Microscopy (CCEM) at McMaster University. Samples were prepared by dropping a suspension of NCs in ethanol onto a copper grid containing lacey Formvar/carbon support film (Ted Pella, Inc).

### *2.3.4: BET Surface area*

BET surface area measurements were done on a Quantachrome Autosorb instrument. All samples were heated to 200 °C with nitrogen as the carrier gas.

### *2.3.5: Scanning Electron Microscopy (SEM)*

Scanning electron microscopy (SEM) with an energy dispersive xray spectroscopy (EDX) were done on LEO 1530 field-emission SEM equipped with Zeiss GeminiSEM. Samples were prepared by adhering to a holder using double sided carbon tape.

### *2.3.6: Photoluminescence*

Photoluminescence spectra were done at room temperature on a Varian Cary Eclipse fluorescence spectrometer. Samples were prepared by adhering powder catalyst to a glass microscope slide using double sided tape. Samples were excited at 285 nm with excitation and emission slits set to 5 nm. 250-395 nm excitation filters and 360-1110 nm emission filters were used during data collection.

### *2.3.7: Time Resolved PL*

Time resolved PL data observes the rate of the DAP emission over a time scale. There can be multiple methods to determine this. In this instance, time resolved PL is done using Time correlated Single Photon Counting (TCSPC). The sample is excited at a

specific wavelength, and a single emission wavelength is observed. Over time, the intensity of the peak would decrease. The amount of time it takes for total decay of the signal can be calculated, and is considered the average lifetime

Time resolved PL data were done using Time Correlated Single Photon Counting (TCSPC) on the Horiba Jobin Yvon IBH Ltd. The samples were irradiated with a 250 nm nanoLED (IBH Ltd.) and the corresponding excitation band maxima was recorded perpendicular to the excitation source. The TCSPC data was collected using a 13 μs measurement range and the decay data was fitted to a biexponential after ~4 points to remove influence from the pulse. The TCSPC data was also collected using a 200 ns measurement range with a 25 kHz repetition rate and fitted to a triexponential function.

## 2.4: Photocatalysis

### *2.4.1: Photocatalysis*

5 mg of catalyst was added to 50 mL of 5 mg/L rhodamine-590 (Rh-590) dye in a 100 mL beaker. The flask was situated ~20 cm under two 40 W 254 nm lamp. The solution was allowed to stir for 30 mins in the dark to ensure an adsorption-desorption equilibrium. After that the solution was exposed to the lamp, where UV-Vis absorption measurements were taken every 10 mins until the Rh-590 peak maximum (520 nm) decreases to zero.

### *2.4.2: Recycling*

Recycling was done by following the previously outlined photocatalysis steps. Then the particles were allowed to settle to the bottom of the flask, taking approximately 2 hours. A 2 mL aliquot was removed from the flask and 2 mL of 12 5mg/L Rh-590 dye was added to the flask to make 5 mg/L solution. The solution was then allowed to stir for 30 mins in dark for adsorption-desorption equilibrium. Then photocatalysis was followed as previously outlined.

### *2.4.3: Scavenger*

Scavenger experiments were done by addition of a scavenger ($FeCl_3$, ascorbic acid, iPro-OH, MeOH) to the solution after 30 mins adsorption-desorption equilibrium to make a 10 mM solution. Then photocatalysis was followed as previously outlined.

# Chapter 3.0: Doped γ-$Ga_2O_3$

## 3.1: Indium Doping

### *3.1.1: Characterization*

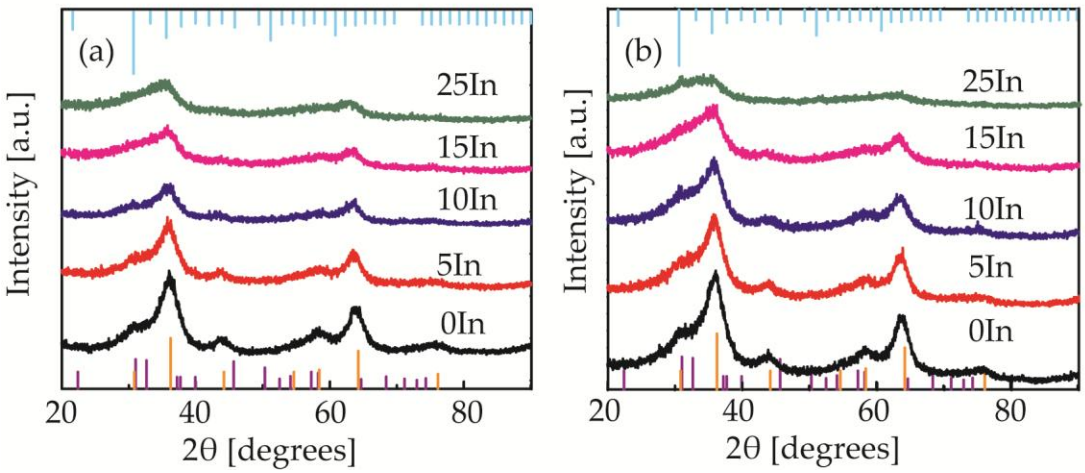


**Figure 3.1: XRD pattern of $Ga_{2-x}In_xO_3$ with concentration of $In^{3+}$ indicated on graph a) as synthesized at 200 °C b) annealed at 400 °C. Light blue ticks are cubic-$In_2O_3$ (JCPDS 06-0416), orange ticks are bulk γ-$Ga_2O_3$ (JCPDS 20-0426), and purple ticks are rh-$In_2O_3$ (JCPDS 22-0336).**

Xray diffraction patterns were collected for as synthesized and annealed samples to ensure that the crystal structure remain consistent with doping. Samples were annealed to remove any surface bound organic ligands such as oleylamine that may occupy the binding sites. In Figure 3.1(a), the as synthesized $Ga_2O_3$ (black coloured trace) matches well with bulk γ-$Ga_2O_3$ (orange coloured trace, JCPDS 20-0426). With addition of 5% indium as a substitutional dopant, the peaks broaden and decrease in intensity (red trace), but the peak position does not shift. With further increase in indium doping

concentration, 10% and 15%, the γ–$Ga_2O_3$ peaks further broaden and decrease in intensity (blue trace and pink trace respectively). This is in good agreement with literature.[45] Therefore, the XRD pattern indicates that the particle size decreases with increasing indium doping concentration, or there is a decrease in crystallinity with increased doping concentration. The ionic radius of $In^{3+}$ (0.080 nm) is much larger than that of $Ga^{3+}$ (0.062 nm), therefore the incorporation of indium into the lattice may expand and increase strain.[46,47] Thus, the particle size is unlikely to decrease with increasing indium incorporation but rather a decrease in crystallinity with increased indium doping due to the difference in ionic radius of the dopant ion.

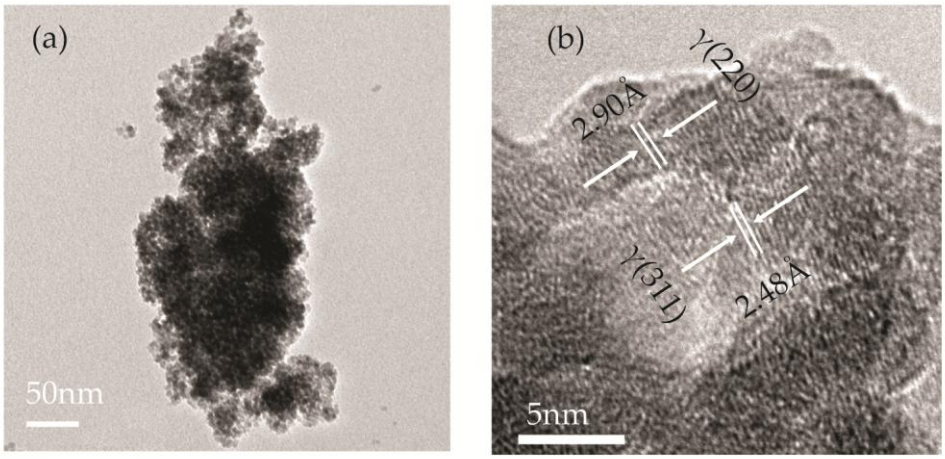


**Figure 3.2: (a) Overview TEM image of $Ga_{1.8}In_{0.2}O_3$ (10 % $In^{3+}$) NCs. (b) High-resolution TEM image of NCs in (a), indicating the lattice spacing corresponding to γ -$Ga_2O_3$ structure.**

The incorporation of indium does not produce discernable $In_2O_3$ peaks (light blue or purple ticks, rhombohedral or cubic respectively), until addition of indium doping concentration at 25% where there are distinct cubic $In_2O_3$ peaks present. Therefore, only 0-15% indium doping concentration was explored to eliminate any potential contribution from a heterojunction or secondary structure(s). The XRD patterns do not change after annealing in Figure 3.1 (b), indicating that the crystal structure is persevered.

TEM imagines were collected to measure the lattice fringes. As demonstrated in Figure 3.2 (a), samples aggregate into clusters after annealing, this occurs consistently in all samples with varying $In^{3+}$ concentrations. The average lattice spacing was also measured and shown in Figure 3.2 (b). The d-spacing was measured to be 2.90 Å and 2.48 Å which corresponds to the (220) and (311) plane respectively which matches well with bulk $\gamma$ - $Ga_2O_3$ values. In addition, energy-dispersive x-ray (EDX) spectroscopy was performed on 5%, 10%, and 15% nominal $In^{3+}$ doping concentration to determine the final doping concentration. The values are listed in Table 1. The final doping concentrations are slightly higher than nominal concentrations, 6.7±1.1%, 10.9±2.2%, and 16.8±1.1% for 5%, 10%, and 15% respectively. Although the final concentrations are slightly higher than starting concentrations, the values are within a reasonable range. In addition, this indicates that doping indium using the previously outlined colloidal synthesis method was efficient.

**Table 1: Summary of final concentration of $In^{3+}$ in the lattice from EDX and specific surface area of $Ga_{2-x}In_xO_3$ from BET measurements**

| Nominal doping concentration (%) | Final concentration (%) | Specific surface area ($m^2/g$) |
|---|---|---|
| 0 | X | 228.5 |
| 5 | 6.7 ± 1.1 | 243.2 |
| 10 | 10.9 ± 2.2 | 252.9 |
| 15 | 16.8 ± 1.1 | 110.1 |

Brunauer–Emmett–Teller (BET) specific surface area measurements were also completed on annealed $Ga_{2-x}In_xO_3$ to monitor any changes in surface area with addition of $In^{3+}$ doping concentration. The values for the specific surface area are summarized in Table 1. Pure γ–$Ga_2O_3$ has a relatively high surface area of 228.5 $m^2/g$ and does not change significantly with indium doping concentration until 15%. 15% indium doping concentration shows a significant drop in surface area, nearly half the value of lower doping concentrations. Conversely, surface area does not change significantly for 300 °C synthesized sample regardless of the doping concentration (appendix, Table A1). Therefore, doping with indium likely does not impact surface area, and is not the only determining factor in impacting rate constants for photocatalysis.

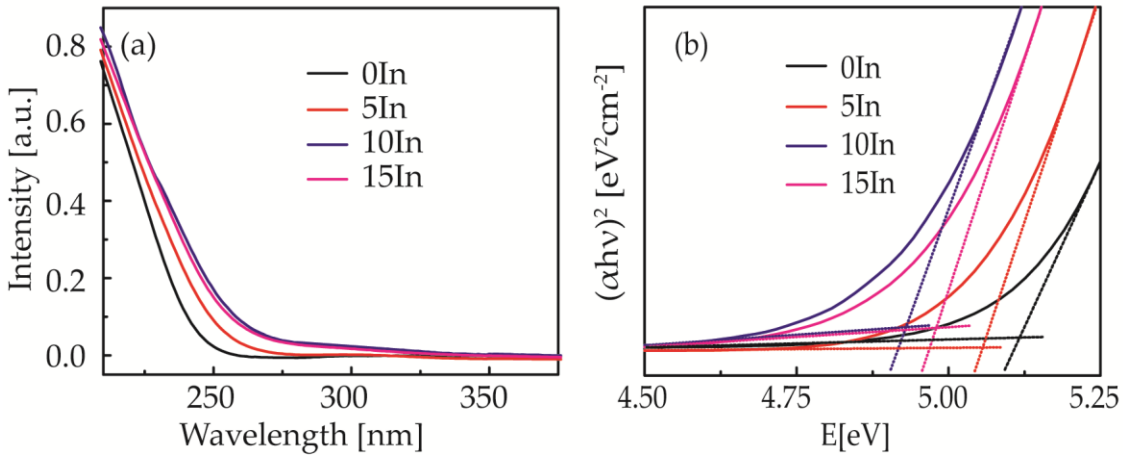


**Figure 3.3: $Ga_{2-x}In_xO_3$ (concentration of $In^{3+}$ indicated on graph) synthesized at 200 °C and dispersed in hexane for a) Absorption spectra of samples in colloidal form, b) Tauc plot calculated from (a) to determine the optical band gap energy.**

UV-Vis absorption measurements were collected to monitor the absorption and to calculate the approximate optical band gap using a tauc plot and presented in Figure 3.3. The absorption red shifts slightly with addition of indium indicating that the band gap energy has shifted to lower energies. This shift is in good agreement with a previous study, however the magnitude of the shift is minimal, and would not have a significant impact on the absorption of the 254 nm light.[45] Therefore, absorption of the 254 nm light would be consistent across all samples.

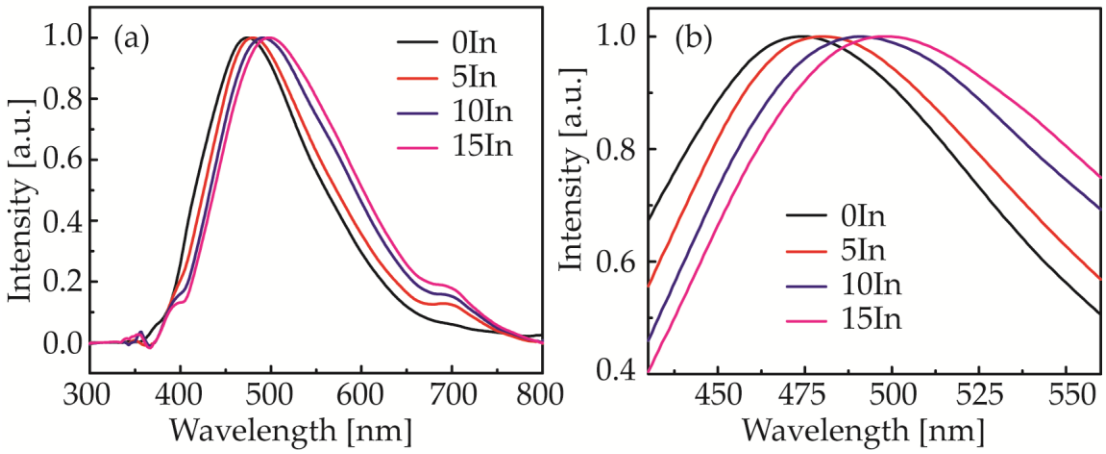


**Figure 3.4: (a,b) Photoluminescence emission spectra of powder $Ga_{2-x}In_xO_3$ synthesized at 200 °C and annealed in air at 400 °C with different $In^{3+}$ doping concentration indicated on graph.**

Photoluminescence (PL) emission was also collected to observe the donor-acceptor-pair (DAP) emission and presented in Figure 3.4. In γ-$Ga_2O_3$, the donor is an oxygen vacancy and the acceptor is a gallium vacancy or gallium-oxygen vacancy.[45,48,49] The DAP emission is a result of donor ($E_d$) and acceptor ($E_a$) vacancy energies, band gap energy ($E_{bg}$), and the Coulombic interaction of the donor and acceptor ($E_c$). [23,48]

$$E=E_{bg} - (E_d + E_a) + E_c \quad (1)$$

Since the band gap term ($E_{bg}$) does not change significantly across samples, only the Coulombic interaction ($E_c$) and the donor ($E_d$) and acceptor ($E_a$) energies would contribute to the DAP energy. The Coulombic interaction is dependent on the average separation distance between donor and acceptor pairs.[49] The DAP emission peak of γ -

$Ga_2O_3$ is centered at 475 nm and red shifts with indium doping concentration toward the emission of $In_2O_3$. [48,49] The red shift in the peak is the evidence of doping $In^{3+}$ into the γ-$Ga_2O_3$ lattice because of the modification of the electronic band structure.[45] The shift in the PL emission to lower energies indicate an increase in average distance between the DAP and/or decrease in concentration of defects. The peaks are also broad indicating a distribution of donor and acceptor states and strong phonon coupling.[23]

### *3.1.2: Lifetime*

Time resolved PL data were also collected on annealed powder samples using the time correlated single photon counting (TCSPC) method measuring the slow (13us) and fast (200 ns) decay of the DAP recombination. A set of runs were done using a 13 μs measurement range to capture the total decay of the DAP emission and shown in Figure 3.5 and would reflect the average separation distance between defects.[50] The decay was fitted to the function;

$$\boldsymbol{F(t) = A + \sum[B_i \exp\left(-\frac{t}{\tau_i}\right)]} \qquad (2)$$

Where $\tau_i$ is the lifetime value and $B_i$ is the relative intensity.[51] The average lifetime can be determined by using the following equation;[51]

$$\boldsymbol{\tau_{avg} = \sum B_i \tau_i} \qquad (3)$$

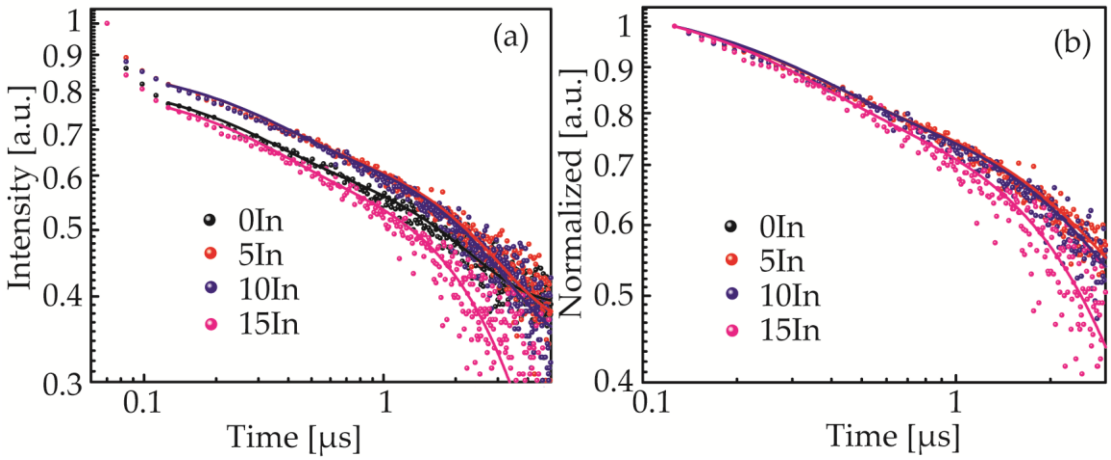


**Figure 3.5: Time-resolved PL data of $Ga_{2-x}In_xO_3$ synthesized at 200 °C and annealed at 400 °C (a) full decay using a 13 us measurement range and fitted to equation 2 using a biexponential function. (b) Normalized after the fast decay from trace (a).**

In Figure 3.5(a) there is a change in time resolved PL decay with $In^{3+}$ doping. With high doping concentration at 15%, the slope of the decay curve becomes slightly steeper and therefore faster recombination time of the DAP. The average lifetime (LT) decreased from 0.43 ± 0.01 μs to 0.41 ± 0.02 μs for 0% and 15% respectively. This is an indicator that there is a small increase in defect concentration with high doping concentration. However, when this decay curve was normalized to the points after the fast decay in Figure 3.5 (b), the slope of the decay does not vary with changing doping concentration. Therefore, the majority of the change in LT is derived from the beginning with the fast decay.

Since the first few points were omitted during fitting of the 13 μs decay process (slow regime), a 200 ns measurement range was also collected for all samples. This

would ensure that the fast decay process was captured at a high resolution. The decay curves were fitted using equation 2 with a triexponential function and the average lifetime values were calculated using equation 3. The decay curves are presented in Figure 3.6, which demonstrate an overall decrease in the average lifetime with increasing $In^{3+}$ doping concentration. The calculated lifetime decreased from 11.0 ± 0.3 ns to 3.4 ± 0.4 ns after doping with 15% indium. Therefore, the decreasing average lifetime would indicate shorter electron or hole trapping time with increasing $In^{3+}$ concentration. Longer average lifetimes may have the highest rate constant since it would be more effective at separating recombination, thus increasing interfacial charge transfer for photocatalysis compared to shorter average LTs. Therefore, the fast decay process may be a method to couple with photocatalysis to observe the defects.

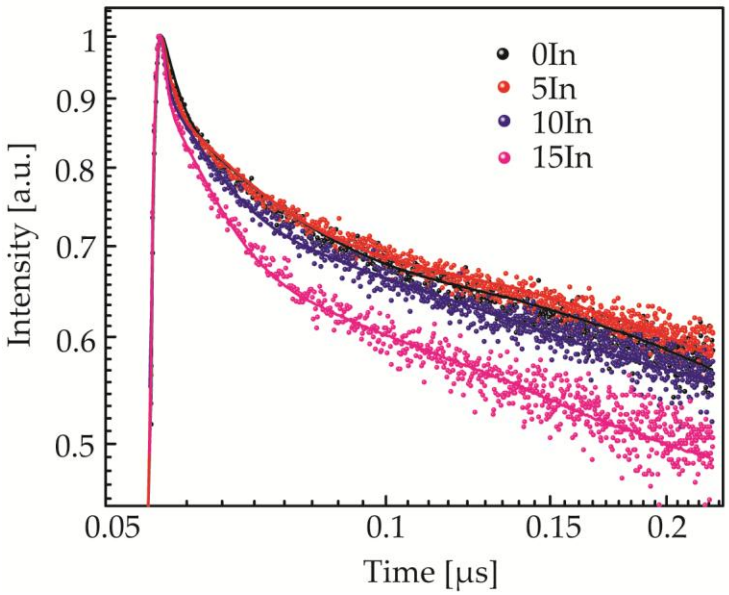


**Figure 3.6: Time resolved PL of $Ga_{2-x}In_xO_3$ synthesized at 200 °C annealed at 400 °C collected by TCSPC method using a 200 ns measurement range. The decays are fitted to a triexponential function.**

### *3.1.3: Photocatalysis*

Photocatalysis was performed for each catalyst exposed to 254 nm light and aqueous rhodamine-590 (Rh-590) dye as the model reactant. Figure 3.7 (a) presents a representative absorption spectra of the reactive species upon increased UV light exposure times with a catalyst. There is a drop in the dye concentration after 30 mins stirring in the dark (red trace) which shows adsorption of dye onto the surface of the catalyst. Control experiments demonstrate that after 30 mins adsorption-desorption equilibrium has been achieved (appendix, Figure A1). This point was determined to be the initial concentration ($C_0$) for kinetic studies. Over time exposure to UV light, the dye

in solution is further degraded, and the peak maximum at 520 nm decreases in intensity. Majority of catalyst samples take 50-60 mins for total degradation of Rh-590. The rate constant was determined using the Langmuir-Hinshelwood model, which is a typical approximation used for semiconductor photocatalysis.[6,7,14,15,33] This follows a pseudo first order model;

$$\ln \frac{C_0}{C} = k_{app}\, t \qquad (4)$$

where $C_0$ the initial concentration, C is the concentration at time $t$, and $k_{app}$ is the apparent rate constant.

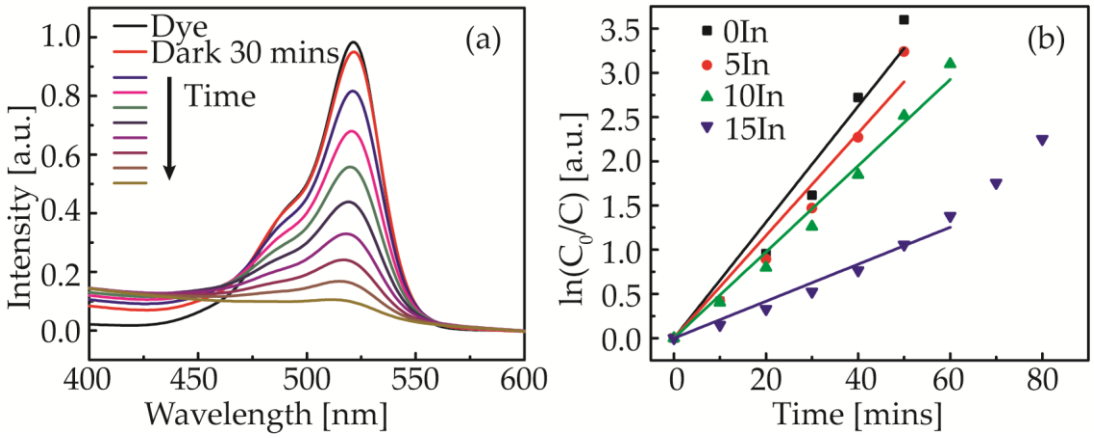


**Figure 3.7: (a) Absorption spectra decay of Rh-590 using $Ga_{1.7}In_{0.3}O_3$(15% $In^{3+}$)synthesized at 200 °C and annealed at 400 °C exposed to 254 nm light using 10 minute exposures per measurement. Black trace is the absorption of dye without catalyst, red trace if the absorption of dye after addition of catalyst with 30 minutes stirring in the dark. (b) Langmuir-Hinshelwood plot of degradation of Rh-590 using $Ga_{2-x}In_xO_3$. The traces were fitted to equation 4.**

The apparent rate constant ($k_{app}$) can be determined from plotting $\ln(C_0/C)$ on the y-axis, and the *t* on the x-axis and fitted to a linear trend. The slope of the linear fit would be the $k_{app}$. This model was only applied to the first few points where the trend remains linear and $R^2$ would be ≥0.99. The Langmuir-Hinshelwood fits were presented in Figure 3.7 (b) which demonstrates the effect of $In^{3+}$ doping concentration on the apparent rate constant. γ-$Ga_2O_3$ (black trace) has a high rate constant, and thus a steep slope. With addition of doping concentration, the slope becomes shallower, and the apparent rate constant drops. Control data were also collected to ensure that the

degradation is a result of the UV light exposure to the catalyst (appendix, Figure A1). Control data include exposure of the dye to UV light without catalyst and catalyst with dye without UV exposure. Both control data showed no degradation of dye, therefore, any degradation of the dye is occurring through the UV-sensitized catalyst.

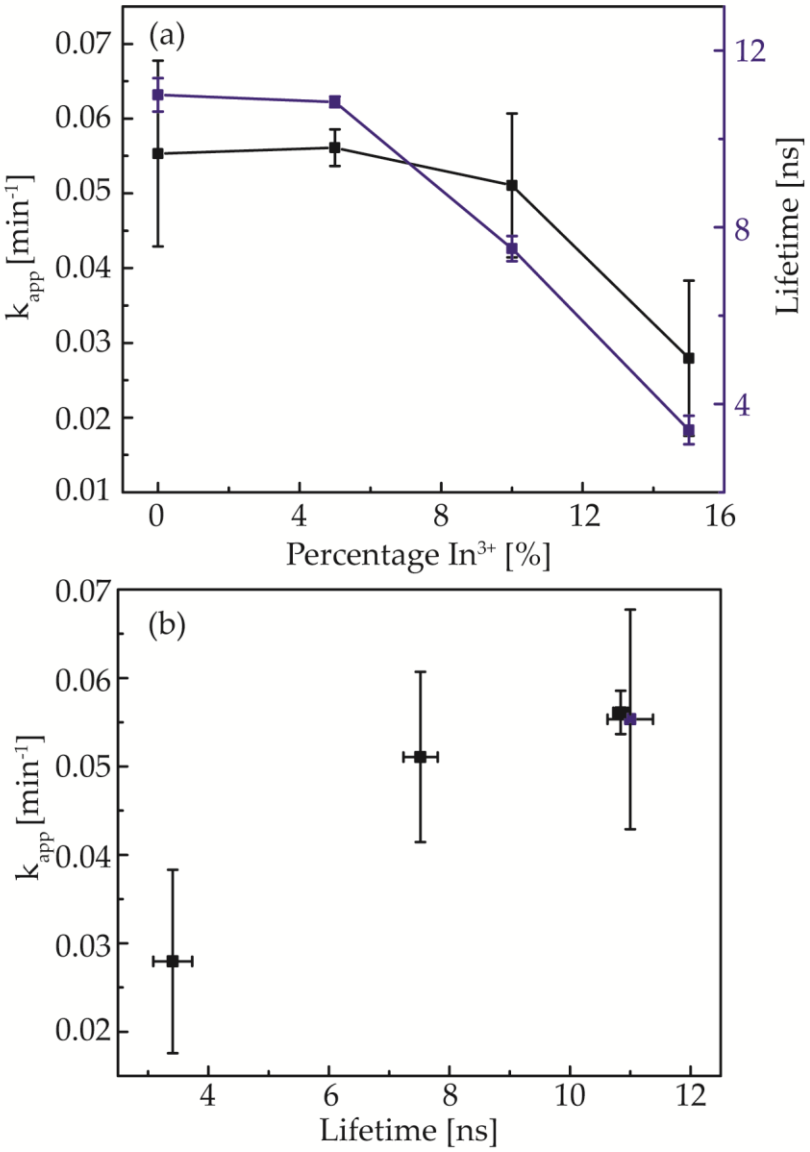


**Figure 3.8: (a) $In^{3+}$ doping percentage dependence of the calculated apparent rate constant of Rh-590 degradation (black squares) and the calculated LT from time resolved PL using 200 ns measurement range (blue squares). (b) LT dependence of apparent rate constant from (a). Blue square represent γ-$Ga_2O_3$, while black squares represent $Ga_{2-x}In_xO_3$.**

Figure 3.8 (a) plots the apparent rate constant and the average lifetimes against nominal percentage $In^{3+}$ concentration. The apparent rate constant (black trace) shows a decrease in value with increase in indium doping concentration. Lifetime using a 200 ns measurement range (blue trace) also follows this trend, where an increase in indium concentration decreases the average lifetime. The fast decay time process observes the DAP recombination time; therefore, a higher doping concentration reduces the trapping time and DAP recombination would increase. Thus, DAP recombination would be in competition with photocatalysis at low LTs or high $In^{3+}$ doping concentrations. This is further proved by plotting the relationship of the LT and apparent rate constant in Figure 3.8 (b). This relationship demonstrates a relative linear relationship between LT and the apparent rate constant.

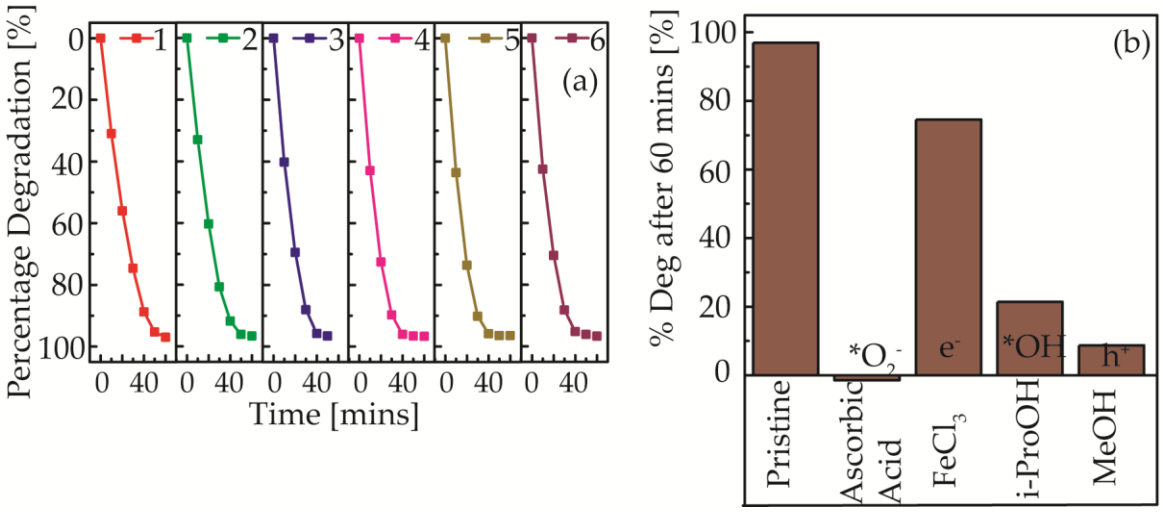


**Figure 3.9: Degradation of Rh-590 using $Ga_{1.7}In_{0.3}O_3$ (15% $In^{3+}$) for (a) over 6 cycles (b) percentage degradation of Rh-590 in presence of various scavengers indicated on the graph.**

This material was able to successfully degrade Rh-590 dye in 60 mins for 6 cycles demonstrated in Figure 3.9 (a). Therefore, this is efficient as a catalyst and doping the material does not impact its stability. In addition, photocatalytic degradation of Rh-590 was performed in the presence of a scavenger as a crude method to approximate the active species and its role during photocatalysis. Demonstrated in Figure 3.9 (b), all tested scavengers decrease the activity of the catalyst from pristine catalyst therefore electron, holes, hydroxyl radicals, and superoxide radicals take an active role in participating in photocatalytic degradation of rh-590. Furthermore, ascorbic acid acts as a superoxide radical scavenger which significantly impacted the photocatalytic activity and displaces the surface bound dye presented as a negative percentage.[52,53] In addition,

in the presence of an electron scavenger, $FeCl_3$, there is a slightly decrease in activity towards the degradation of Rh-590.[54] Comparing the difference in impact between those two scavengers suggest that the role of the electron may primarily be the generation of radicals. Furthermore, isopropanol is a known hydroxyl radical scavenger and demonstrated that there is a significant inhibition of the photocatalytic activity.[55] In addition, the introduction of methanol, a known hole scavenger, decreases the photocatalytic activity as well. [56–58] Therefore, majority of reactive species play an active role in the photocatalytic degradation of Rh-590 most notably the radicals and holes.

## 3.2: Zinc Doping

### *3.2.1: Characterization*

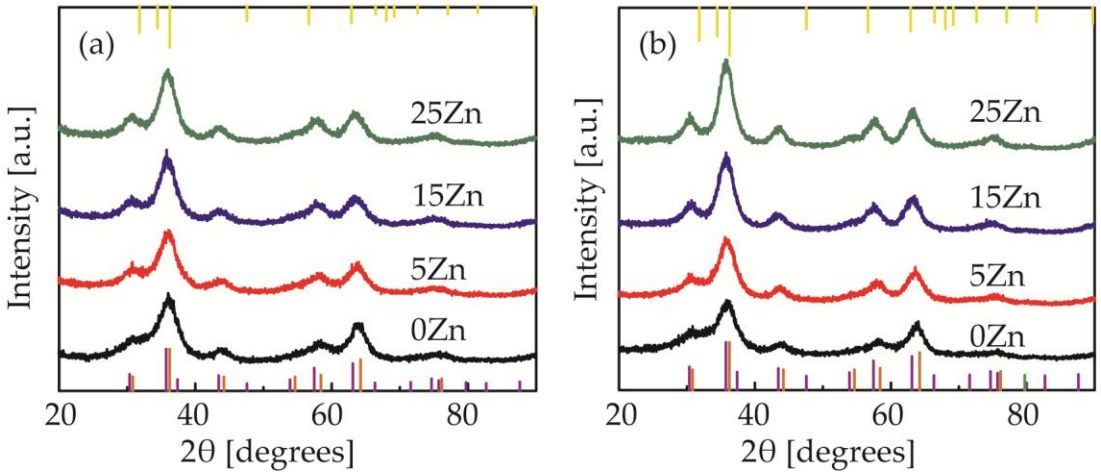


**Figure 3.10: XRD patterns of $Ga_{2-x}Zn_xO_3$ (a) as synthesized at 200 °C (b) annealed at 400 °C. Yellow coloured ticks are ZnO (JCPDS 36-1451), purple coloured ticks are $ZnGa_2O_4$ (JCPDS 38-1240), orange coloured ticks are γ-$Ga_2O_3$ (JCPDS 20-0426).**

To further explore the impact of doping, γ-$Ga_2O_3$ was doped with $Zn^{2+}$. $Ga_{2-x}Zn_xO_3$ was synthesized using the colloidal method previously outlined. The XRD pattern of as synthesized and annealed samples shown in Figure 3.11 demonstrates that doped samples were successfully synthesized. The as synthesized $Ga_{1.9}Zn_{0.1}O_3$ (5% $Zn^{2+}$) in Figure 3.10 (a) (red trace) match well with bulk γ- $Ga_2O_3$ (orange ticks, JCPDS 20-0426). Further $Zn^{2+}$ doping of the as synthesized samples does not show a significant change in majority of the peak intensity or position. However, some peaks, such as at 35 degrees, has a slight increase in intensity with increased doping concentration which may indicate a preferential growth direction with a dopant present during synthesis.

After annealing the samples at 400 °C shown in Figure 3.10 (b), the peak intensity increases and narrows with increased doping concentration. This may indicate that annealing has increased the size of the particles or increased crystallinity with higher doping concentrations. Similar to $In^{3+}$, incorporation of $Zn^{2+}$ into the host lattice would add strain the structure since $Zn^{2+}$ (0.074 nm) has a slightly larger ionic radius than $Ga^{3+}$ (0.062 nm).[46] A peak shift at 65 degrees to lower angles was noted at 25% zinc doping concentration relative to bulk $\gamma$-$Ga_2O_3$. This shift may be attributed to formation of $ZnGa_2O_4$ (purple coloured ticks, JCPDS 38-1240) or the strain from incorporation of $Zn^{2+}$ into the lattice. $ZnGa_2O_4$ also has a spinel crystal structure and highly stable, thus it seems likely that there may be some $ZnGa_2O_4$ formation occurring.[59–61] However the peaks for bulk $ZnGa_2O_4$ are very close to bulk $\gamma$-$Ga_2O_3$ thus making it hard to determine when this formation occurs. Furthermore, there are no peaks that match those of bulk ZnO (yellow coloured ticks, JCPDS 36-1451); therefore there are no formation of ZnO regardless of the concentration of $Zn^{2+}$. Therefore, there could either be a co-formation of the $ZnGa_2O_4$ and $\gamma$ -$Ga_2O_3$ to form a junction or conversion of $\gamma$-$Ga_2O_3$ to $ZnGa_2O_4$. Thus, 25% $Zn^{2+}$ doped sample was omitted since this concentration is close to the stoicheometric ratio to form $ZnGa_2O_4$.

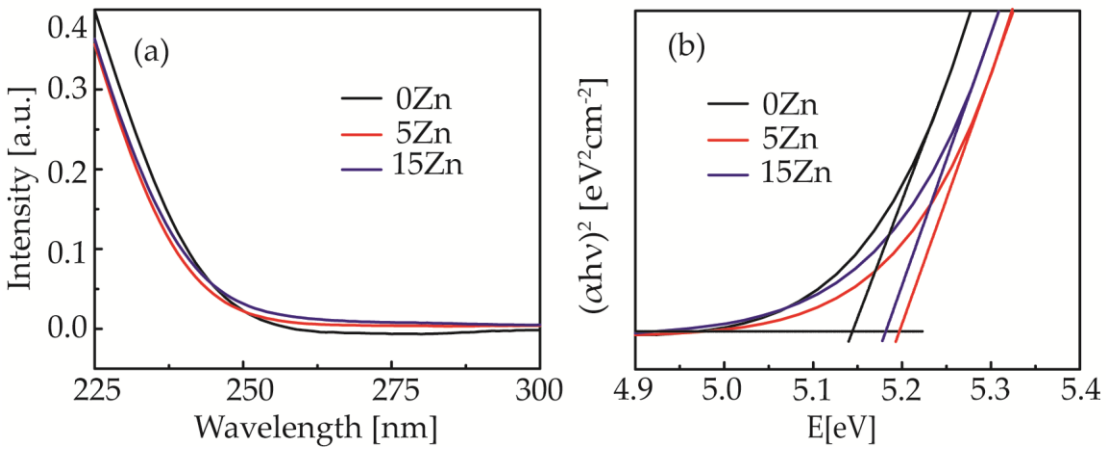


**Figure 3.11: $Ga_{2-x}Zn_xO_3$ synthesized at 200 °C and dispersed in hexane for (a) UV-Vis absorption spectra (b) Tauc plot calculated from (a).**

UV-Vis absorption data was collected and the optical band gap can be calculated which are shown in Figure 3.11. The absorption spectrum in Figure 3.11(a) displays little change in absorption with increasing $Zn^{2+}$ doping concentration. As a result, the band gap energy would also remain consistent with addition of zinc doping concentration since the difference is ~0.03 eV which is marginal. Furthermore, this material would have similar absorption efficiency of the 254 nm light with various doping concentrations since the absorption band does not change significantly.

**Table 2: Summary table of $Ga_{2-x}Zn_xO_3$ synthesized at 200 °C and annealed at 400 °C for final concentration of $Zn^{3+}$ determined from EDX and specific surface area from BET.**

| Nominal doping percentage (%) | Final Percentage $Zn^{2+}$ (%) | Specific surface area ($m^2/g$) |
|---|---|---|
| 0 | X | 228.5 |
| 5 | 4.2 ± 0.2 | 145.2 |
| 15 | 11.3 ± 3.3 | 319.8 |

The final doping concentration of $Ga_{2-x}Zn_xO_3$ was determined using EDX. The final concentrations are presented in Table 2. 4.2 ± 0.2% and 11.3 ± 3.3% are the final doping concentrations for 5% and 15% respectively. The final doping concentrations are close to that of starting. Therefore, doping $Zn^{2+}$ using a colloidal synthesis method was efficient as the final concentrations are close to that of starting concentrations.

Specific surface area of the particles was determined using BET and displayed in Table 2. The surface areas between the different $Zn^{2+}$ doping concentrations are significantly different and do not follow a clear trend. This may impact photocatalysis since surface area signifies available binding sites. If surface area was a significant factor in effecting photocatalysis then 15% $Zn^{2+}$ doping concentration would have the highest rate constant since it has the highest surface area. However, this would be proven not to be the case during photocatalytic studies. Therefore, surface area would not be the sole factor in impacting photocatalysis.

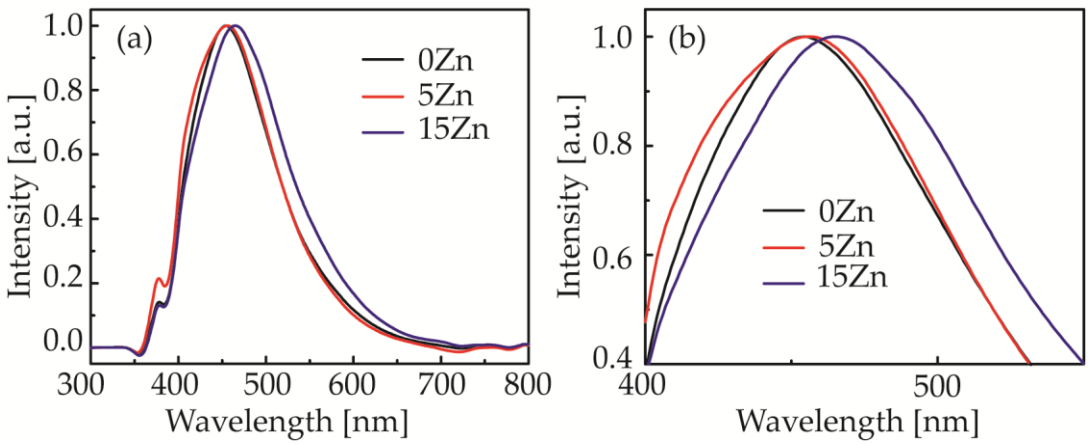


**Figure 3.12: (a,b) Photoluminescence emission spectra of different concentrations of $Ga_{2-x}Zn_xO_3$ synthesized at 200 °C and annealed in air at 400 °C. Doping concentrations are indicated on graph.**

The band structure of the samples were observed using PL emission and time-resolved PL. PL data was collected for all samples to determine the recombination of electron and holes previously described, often from the DAP recombination. The spectrum for powder samples are displayed in Figure 3.12 which shows broad emission peaks indicating strong phonon coupling and/or a broad distribution of donor and acceptor states. As previously discussed, the PL emission is derived from the Coulombic interaction, donor and acceptor energies, and the band gap energy formulated in equation 1. Between the different doping concentrations, powder PL emission demonstrates a 9 nm increase in the peak wavelength when doping from 5% to 15%. Furthermore, the red shift for the PL emission indicates that there is a shift to

lower energies, therefore there is an increase in DAP distance and/or a decrease in defect concentration based off equation 1 shown previously. Since there is not a significant change in the band gap, this PL peak shift is most likely derived from a decrease in defect concentration.

### *3.2.2: Lifetime*

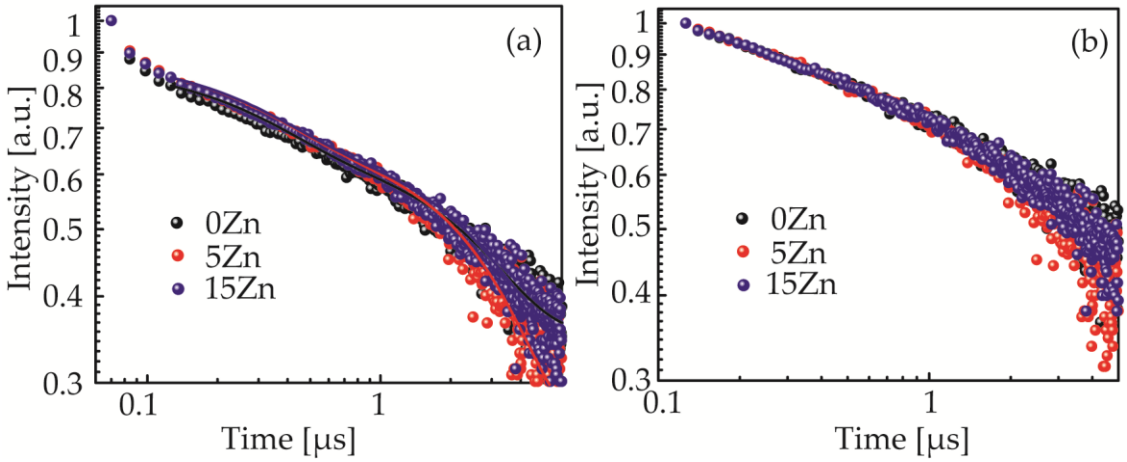


**Figure 3.13: Time resolved PL using a 13 μs measurement range of $Ga_{2-x}Zn_xO_3$ synthesized at 200 °C and annealed at 400 °C (a) full decay fitted to equation 2 using a biexponential function after 4 points (b) normalized to only the fitted portion of (a).**

Time resolved PL data were collected by TCSPC for each sample to determine the lifetime of the electron and hole recombination. Similar to indium doped samples, full decay (13 μs) of the DAP recombination were collected and presented in Figure 3.13. First, the slow decay curves initially indicate that there is an increase in average lifetime

with addition of zinc doping concentration as shown in Figure 3.13 (a). This indicates that there is a decrease in DAP recombination and therefore a decrease in defect concentration. The calculated LT increased from 0.43 ± 0.01 μs to 0.45 ± 0.02 μs after 15% $Zn^{2+}$ doping. However, when the plots were normalized to the points after the fast decay, Figure 3.13(b) demonstrates that the slope of the decay does not change between different samples. Therefore, similar to indium doped samples, majority of the change in LT is derived from the beginning with the fast decay. Therefore, further proof that measuring the fast decay at the beginning may be more effective at determining charge separation efficiency.

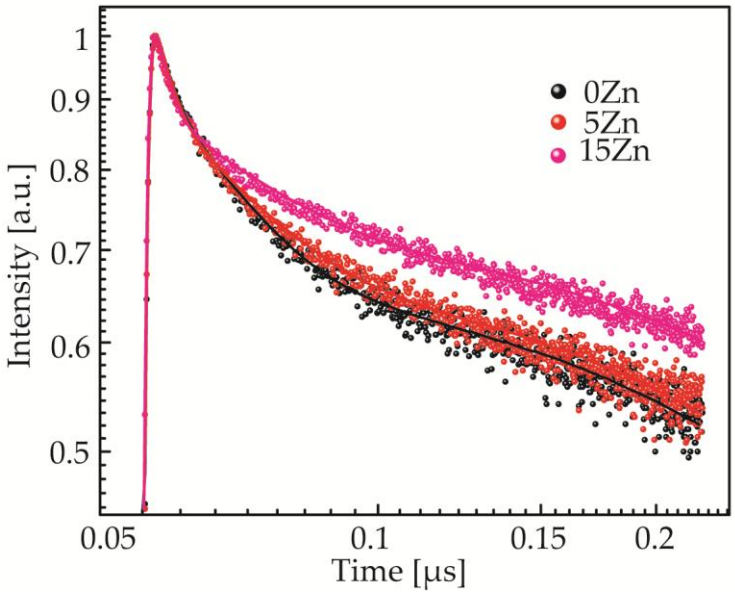


**Figure 3.14: Time resolved PL using a 200 ns measurement range of $Ga_{2-x}Zn_xO_3$ synthesized at 200 °C and annealed at 400 °C.**

Following, fast decay of the lifetime was collected for each sample and presented in Figure 3.14. The curves are fitted to a triexponential function equation 2 to obtain $B_i$ and $\tau_i$ variables. The average lifetime is calculated from equation 3 using the variables determined from the fit in equation 2. The fast regime decay curves in Figure 3.14 (a) show an increase in average lifetime with 15% $Zn^{2+}$ doping concentration from 11.0 ± 0.3 ns to 15.1 ± 0.4 ns . This is the opposite trend that is seen with indium doping. The average LT would determine the trapping time of electrons and holes on the DAP or the DAP recombination time. Therefore, higher $Zn^{2+}$ doping concentration would mitigate DAP recombination and increase photocatalysis because of a higher probability for interfacial charge transfer or charge carrier trapping by surface species.

*3.2.3: Photocatalysis*

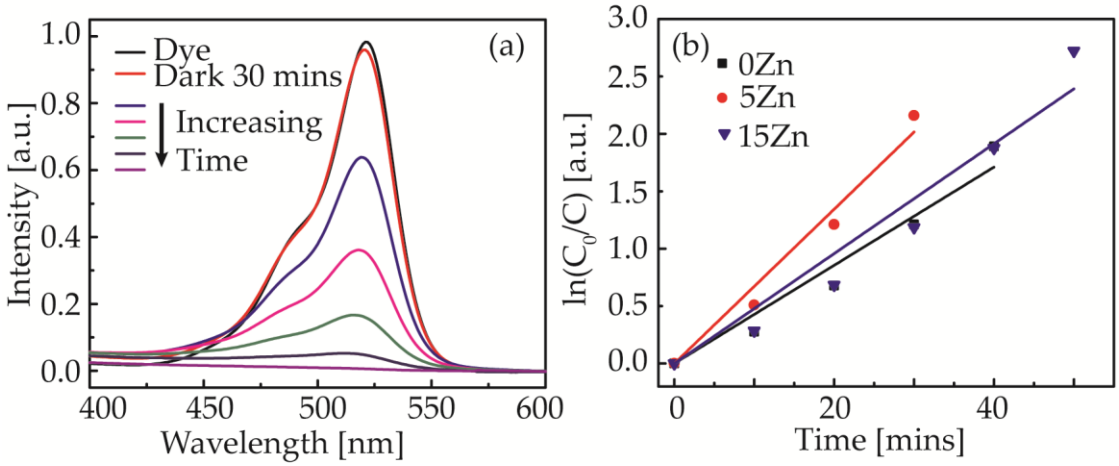


**Figure 3.15: (a) Absorption spec of decay of Rh-590 for $Ga_{1.7}Zn_{0.3}O_3$ (15%zinc) synthesized at 200 °C and annealed at 400 °C, with 10 minute exposure increments to UV per measurement. Black trace is the absorption of dye without catalyst, red trace is after addition of catalyst with 30 minutes of stirring in the dark. (b) Langmuir-Hinshelwood plot of degradation of Rh-590 using $Ga_{2-x}Zn_xO_3$.**

Photocatalytic degradation of aqueous Rh-590 was conducted on all catalyst in triplicate using a 254 nm light. Figure 3.15 (a) presents a typical absorption spectra of degradation of Rh-590 in the presence of a catalyst that one may expect to observe. These sets of data are fitted to the Langmuir-Hinshelwood model, equation 4, previously outlined to determine the rate constant as shown in Figure 3.15(b).

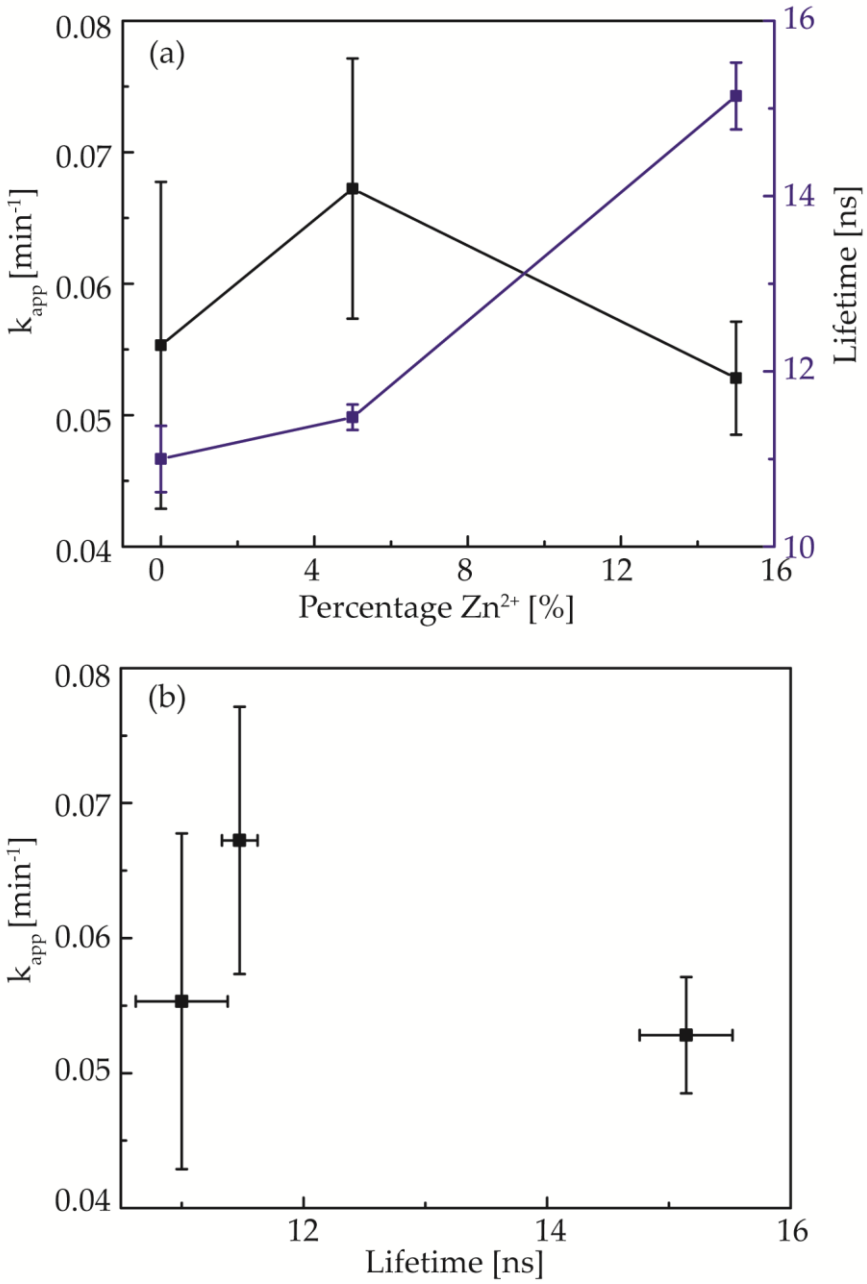


**Figure 3.16: a) $Zn^{2+}$ doping percentage dependence of the calculated apparent rate constant of Rh-590 degradation (black squares) and the calculated LT from time resolved PL using 200 ns measurement range (blue squares). (b) LT dependence of apparent rate constant from (a).**

The calculated rate constants of the photocatalytic data for $Ga_{2-x}Zn_xO_3$ are presented in Figure 3.16(a) to determine the relationship between doping concentration and the rate constant (black trace) as well as the lifetime (blue trace). Majority of these samples take 50-60 mins to completely degrade Rh-590. With increased doping concentration, there is an increase in apparent rate constant for photocatalysis up to a maximum. This trend correlates with the average lifetime of the fast decay regime where an increase in LT increases photocatalysis due to increase in probability for interfacial charge transfer. Therefore, it is likely that observing a fast LT can help determine relative efficiency of photocatalysis. However, the rate constant does not significantly increase at 15% where the LT is significantly increased. This may indicate that DAP recombination is no longer in competition with photocatalysis. This is further proven when observing the relationship between lifetime and apparent rate constant in Figure 3.16(b). The rate constants are fairly similar despite the differing lifetimes.

# Chapter 4.0: Conclusion and Future work

## 4.1: Conclusion

$Ga_{2-x}M_xO_3$ ($M=In^{3+}$ or $Zn^{2+}$) was successfully synthesized using the colloidal synthesis method. The nanoparticles would adopt the defect spinel structure of γ-$Ga_2O_3$. Different dopant ions would manipulate the host lattice in different ways. Collectively, the specific surface area from BET measurements did not change consistently with doping concentration however it was noted that specific surface area seems to coincide better with LT rather than $k_{app}$. This may indicate that the defects are located primarily in the vicinity of the surface, and are more readily expelled with annealing in the process of preparing the catalyst.[48] However, the crystal structure may behave differently depending on the size and charge of the dopant after annealing. For instance, doping with $In^{3+}$, a significantly larger ion compared to $Ga^{3+}$, adds strain to the crystal structure resulting in a decrease in XRD peak intensity with an increase in dopants. However $Zn^{2+}$ is slightly larger than $Ga^{3+}$ and does not modify the crystal structure significantly based off of XRD data. The XRD diffraction patterns remain relatively consistent with addition of $Zn^{2+}$ dopant however there was an increase in crystallinity after annealing. However, $ZnGa_2O_4$ was formed at high doping concentrations due to the increased stability of the spinel crystal structure compared to γ- $Ga_2O_3$.

Moreover, the absorption and by extension the optical band gap is modified with dopants. The band gap shrinks with addition of $In^{3+}$ however; there is little change to the band gap with addition of $Zn^{2+}$. On the other hand, the change in band gap for $In^{3+}$ doped samples was considered negligible since the change was minimal. In addition, the photoluminescence emission would red shift with increasing doping concentrations regardless of the dopant ion. However, the magnitude of the shift would be impacted. $In^{3+}$ doped samples has a ca. 24 nm shift while $Zn^{2+}$ doped samples has a ca. 9 nm shift from $\gamma$- $Ga_2O_3$ to $Ga_{1.7}M_{0.3}O_3$ (M=$In^{3+}$ or $Zn^{2+}$). Since the band gap does not change significantly, the shift in PL emission was most likely derived from the increase in DAP distance or decrease in defect concentration.

Furthermore, the lifetime of the samples were impacted differently with dissimilar dopant ions. Measuring the total LT decay at 13 μs, $Ga_{2-x}In_xO_3$ generally decreased the LT while $Ga_{2-x}Zn_xO_3$ increased the LT with increasing doping concentration. However, the total LT decay at 13 μs does not give sufficient resolution to determine the changes with the defect concentration or DAP recombination. Majority of the changes in lifetime occur at the beginning of the decay. Therefore, measuring the initial fast decay at 200 ns would provide more information on the DAP recombination relative to the photocatalytic activity.

Different dopant ions would increase or decrease the average fast lifetime regime. For instance, indium decreases LT to 3.4 ± 0.4 ns from 11.0 ± 0.3 ns with increasing doping concentration while zinc increases LT to 15.1 ± 0.4 ns with increasing doping concentration. This can be a method to tune the LT and thus manipulate the DAP trapping time. There is also an impact on the photocatalysis, where there is a positive correlation between the LT and the apparent rate constant as shown in Figure 3.17. However, photocatalysis was not impacted significantly at extremely high LT values beyond ca. 8 ns where a plateau is present. The plateau may indicate that there was a maximum LT threshold for DAP recombination to impact photocatalysis. Therefore, if the LT were below 8 ns then the DAP recombination would be a significant competitor to photocatalysis. This may indicate that one of the processes during photocatalysis, such as charge transfer to reactive species, would take ca. 8 ns to occur since LTs below that value severely impact photocatalysis. Therefore, further prolonging DAP trapping time beyond 8 ns would not significantly impact photocatalysis as there may be other factors that may affect this reaction.

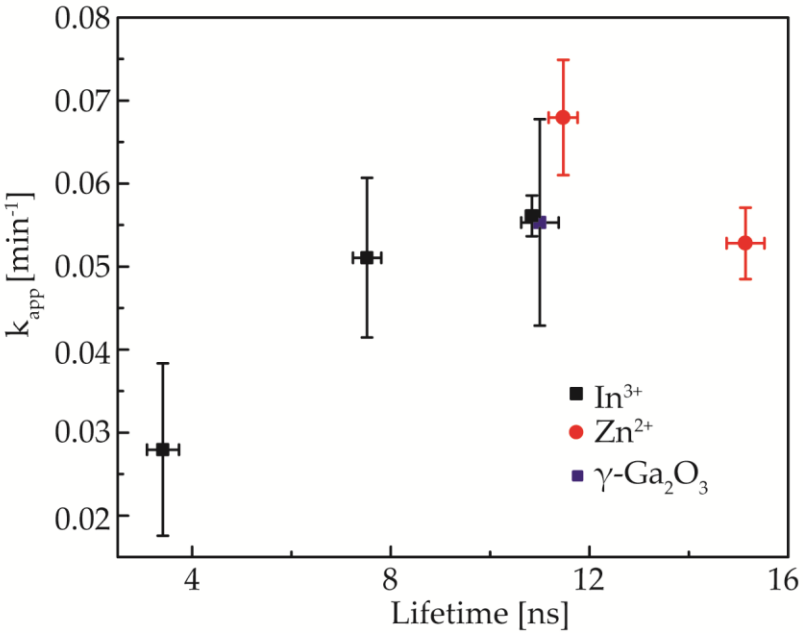


**Figure 3.17: LT dependence of apparent rate constant for $Ga_{2-x}M_xO_3$ (M=$In^{3+}$ or $Zn^{2+}$). LT calculated from the 200 ns time resolved PL spectra. The apparent rate constant is calculated from the degradation of Rh-590 using a Langmuir-Hinshelwood plot. Blue point represents γ-$Ga_2O_3$. Black points represent $Ga_{2-x}In_xO_3$. Red points represent $Ga_{2-x}Zn_xO_3$.**

These differences in LT between different dopant ions may be attributed to occupying different coordination sites in the host lattice. γ- $Ga_2O_3$ has both octahedral and tetrahedral coordination sites; therefore, the dopant ion is able to occupy either of those sites. $Zn^{2+}$ would preferentially occupy the tetrahedral coordination sites while $In^{3+}$ would prefer octahedral coordination sites. Thus, the difference in the electronic band structure for different dopant ions may originate from occupation of different coordination sites.

In conclusion, doping semiconductors can be a method to tune the defects, and be able to manipulate the photocatalysis. The DAP recombination from defects can be monitored using LT calculated from the TCSPC method for time resolved PL. There is a positive correlation between the LT and the apparent rate constant for photocatalysis up to a plateau where the DAP recombination would not be a significant factor.

## 4.2: Future Work

Given that there is evidence of different dopants ions manipulating defects differently, however what remains to be unknown is why. One such direction is to explore how different preferential coordinations of the dopant ion may contribute to the electronic band structure and the apparent rate constant for photocatalysis. Since gallium oxide contains both octahedral and tetrahedral sites, either can be occupied by the dopant ion. For instance, $Co^{2+}$ would preferentially occupy the tetrahedral coordination site similar to $Zn^{2+}$ while $Ni^{2+}$ would preferentially occupy the octahedral coordination site similar to indium. The ionic radii of $Co^{2+}$ and $Ni^{2+}$ are both 0.07 nm which is slightly larger than that of $Ga^{3+}$ at 0.062nm.[46,47] As a result, the strain added to the lattice would be consistent between the two dopant ions. Currently, there is evidence that indium occupies the octahedral coordination in the $\gamma$-$Ga_2O_3$ lattice using X-ray absorption spectroscopy (XAS).[45] Therefore, XAS data would be collected to verify this hypothesis. If there are consistent correlations between the coordination of the

dopant ion and the activity then this may be another method to tune similar materials for different applications.

Another set of experiments to be done would be observing the impact of different synthesis and/or annealing environments on defects and consequently, photocatalysis. Currently, the colloidal synthesis process undergoes an inert atmosphere in argon, and the collected product is annealed in air. However, if the sample were to be annealed in argon, there should be more oxygen vacancies when annealed in argon compared to annealing in air and thus increase photocatalysis.[62] A reducing environment such as hydrogen may also be included in the series of annealing experiments to further induce defects. The synthesis environment may be modified to increase or decrease vacancies. This can be done by addition of hydrogen during synthesis for a reducing environment to increase vacancies, or oxygen as an oxidizing environment to reduce vacancies. A previous study by Wang et al (2011) demonstrated that PL intensities was greater when in a reducing environment versus an oxidizing environment.[49] Therefore, this may be an interesting area to modify vacancies and determine the impact on photocatalysis.

# References


1. Grundmann, M. *The Physics of Semiconductors: An Introduction Including Nanophysics and Applications*. (Springer, 2015).
2. Alivisatos, A. P. Semiconductor Clusters, Nanocrystals, and Quantum Dots. *Science* **271,** 933–937 (1996).
3. Coutts, T. J., Young, D. L. & Li, X. Characterization of Transparent Conducting Oxides. *MRS Bulletin* **25,** 58–65 (2000).
4. Lewis, B. G. & Paine, D. C. Applications and Processing of Transparent Conducting Oxides. *MRS Bulletin* **25,** 22–27 (2000).
5. Ginley, D. S. & Bright, C. Transparent Conducting Oxides. *MRS Bulletin* **25,** 15–18 (2000).
6. Fujishima, A., Zhang, X. & Tryk, D. A. TiO2 photocatalysis and related surface phenomena. *Surface Science Reports* **63,** 515–582 (2008).
7. Hoffmann, M. R., Martin, S. T., Choi, W. & Bahnemann, D. W. Environmental Applications of Semiconductor Photocatalysis. *Chem. Rev.* **95,** 69–96 (1995).
8. Espitia, P. J. P. *et al.* Zinc Oxide Nanoparticles: Synthesis, Antimicrobial Activity and Food Packaging Applications. *Food Bioprocess Technol* **5,** 1447–1464 (2012).
9. Pirkanniemi, K. & Sillanpää, M. Heterogeneous water phase catalysis as an environmental application: a review. *Chemosphere* **48,** 1047–1060
10. Schneider, J. *et al.* Understanding TiO2 Photocatalysis: Mechanisms and Materials. *Chem. Rev.* **114,** 9919–9986 (2014).
11. Park, H., Kim, H., Moon, G. & Choi, W. Photoinduced charge transfer processes in solar photocatalysis based on modified TiO 2. *Energy & Environmental Science* **9,** 411–433 (2016).

12. Chan, S. H. S., Yeong Wu, T., Juan, J. C. & Teh, C. Y. Recent developments of metal oxide semiconductors as photocatalysts in advanced oxidation processes (AOPs) for treatment of dye waste-water. *J. Chem. Technol. Biotechnol.* **86,** 1130–1158 (2011).

13. Ibhadon, A. O. & Fitzpatrick, P. Heterogeneous Photocatalysis: Recent Advances and Applications. *Catalysts* **3,** 189–218 (2013).

14. Lachheb, H. *et al.* Photocatalytic degradation of various types of dyes (Alizarin S, Crocein Orange G, Methyl Red, Congo Red, Methylene Blue) in water by UV-irradiated titania. *Applied Catalysis B: Environmental* **39,** 75–90 (2002).

15. Kudo, A. & Miseki, Y. Heterogeneous photocatalyst materials for water splitting. *Chem. Soc. Rev.* **38,** 253–278 (2008).

16. Zhang, X. *et al.* Effect of aspect ratio and surface defects on the photocatalytic activity of ZnO nanorods. *Scientific Reports* **4,** (2014).

17. Grundmann, P. D. M. in *The Physics of Semiconductors* 347–378 (Springer Berlin Heidelberg, 2010). doi:10.1007/978-3-642-13884-3_11

18. Zheng, L. *et al.* Network Structured SnO2/ZnO Heterojunction Nanocatalyst with High Photocatalytic Activity. *Inorg. Chem.* **48,** 1819–1825 (2009).

19. Wang, L. *et al.* 3D porous ZnO–SnS p–n heterojunction for visible light driven photocatalysis. *Physical Chemistry Chemical Physics* **19,** 16576–16585 (2017).

20. Kong, M. *et al.* Tuning the Relative Concentration Ratio of Bulk Defects to Surface Defects in TiO2 Nanocrystals Leads to High Photocatalytic Efficiency. *J. Am. Chem. Soc.* **133,** 16414–16417 (2011).

21. Radoičić, M. B. *et al.* The role of surface defect sites of titania nanoparticles in the photocatalysis: Aging and modification. *Applied Catalysis B: Environmental* **138–139,** 122–127 (2013).

22. Yan, J. *et al.* Understanding the effect of surface/bulk defects on the photocatalytic activity of TiO2: anatase versus rutile. *Phys. Chem. Chem. Phys.* **15,** 10978–10988 (2013).

23. Wang, T. & Radovanovic, P. V. Size-Dependent Electron Transfer and Trapping in Strongly Luminescent Colloidal Gallium Oxide Nanocrystals. *J. Phys. Chem. C* **115,** 18473–18478 (2011).

24. Ghodsi, V., Jin, S., Byers, J. C., Pan, Y. & Radovanovic, P. V. Anomalous Photocatalytic Activity of Nanocrystalline γ-Phase Ga2O3 Enabled by Long-Lived Defect Trap States. *J. Phys. Chem. C* **121,** 9433–9441 (2017).

25. Wang, X. *et al.* Photocatalytic Overall Water Splitting Promoted by an α–β phase Junction on Ga2O3. *Angew. Chem. Int. Ed.* **51,** 13089–13092 (2012).

26. Jin, S. *et al.* Effect of Phase Junction Structure on the Photocatalytic Performance in Overall Water Splitting: Ga2O3 Photocatalyst as an Example. *J. Phys. Chem. C* **119,** 18221–18228 (2015).

27. King, P. D. C. *et al.* Band gap, electronic structure, and surface electron accumulation of cubic and rhombohedral In2O3. *Phys. Rev. B* **79,** 205211 (2009).

28. Farvid, S. S. & Radovanovic, P. V. Phase Transformation of Colloidal $In_2O_3$ Nanocrystals Driven by the Interface Nucleation Mechanism: A Kinetic Study. *Journal of the American Chemical Society* **134,** 7015–7024 (2012).

29. Bierwagen, O. Indium oxide—a transparent, wide-band gap semiconductor for (opto)electronic applications. *Semicond. Sci. Technol.* **30,** 024001 (2015).

30. Chen, X., Shen, S., Guo, L. & Mao, S. S. Semiconductor-based Photocatalytic Hydrogen Generation. *Chem. Rev.* **110,** 6503–6570 (2010).

31. Kudo, A. & Mikami, I. Photocatalytic activities and photophysical properties of Ga2−xInxO3 solid solution. *J. Chem. Soc., Faraday Trans.* **94,** 2929–2932 (1998).

32. Kumar, K. J., Raju, N. R. C. & Subrahmanyam, A. Thickness dependent physical and photocatalytic properties of ITO thin films prepared by reactive DC magnetron sputtering. *Applied Surface Science* **257,** 3075–3080 (2011).

33. Samadi, M., Zirak, M., Naseri, A., Khorashadizade, E. & Moshfegh, A. Z. Recent progress on doped ZnO nanostructures for visible-light photocatalysis. *Thin Solid Films* **605,** 2–19 (2016).

34. Kumar, R., Anandan, S., Hembram, K. & Narasinga Rao, T. Efficient ZnO-Based Visible-Light-Driven Photocatalyst for Antibacterial Applications. *ACS Appl. Mater. Interfaces* **6,** 13138–13148 (2014).

35. Özgür, Ü. *et al.* A comprehensive review of ZnO materials and devices. *Journal of Applied Physics* **98,** 041301 (2005).

36. Daneshvar, N. Photocatalytic degradation of azo dye acid red 14 in water on ZnO as an alternative catalyst to TiO2. *Journal of Photochemistry and Photobiology A: Chemistry* **162,** 317–322

37. Zhang, X. *et al.* Carbon-Doped ZnO Nanostructures: Facile Synthesis and Visible Light Photocatalytic Applications. *J. Phys. Chem. C* **119,** 20544–20554 (2015).

38. Rehman, S. Strategies of making TiO2 and ZnO visible light active. *Journal of Hazardous Materials* **170,** 560–569 (2009).

39. Bryan, J. D. & Gamelin, D. R. in *Progress in Inorganic Chemistry* (ed. Karlin, K. D.) 47–126 (John Wiley & Sons, Inc., 2005).

40. Norris, D. J., Efros, A. L. & Erwin, S. C. Doped Nanocrystals. *Science* **319,** 1776–1779 (2008).

41. Dalpian, G. M. & Chelikowsky, J. R. Self-Purification in Semiconductor Nanocrystals. *Phys. Rev. Lett.* **96,** 226802 (2006).

42. Zhang, H., Chen, G. & W. Bahnemann, D. Photoelectrocatalytic materials for environmental applications. *Journal of Materials Chemistry* **19,** 5089–5121 (2009).

43. Piyadasa, A., Wang, S. & Gao, P.-X. Band structure engineering strategies of metal oxide semiconductor nanowires and related nanostructures: A review. *Semicond. Sci. Technol.* **32,** 073001 (2017).

44. Paramasivam, I., Jha, H., Liu, N. & Schmuki, P. A Review of Photocatalysis using Self-organized TiO2 Nanotubes and Other Ordered Oxide Nanostructures. *Small* **8,** 3073–3103 (2012).

45. Farvid, S. S., Wang, T. & Radovanovic, P. V. Colloidal Gallium Indium Oxide Nanocrystals: A Multifunctional Light-Emitting Phosphor Broadly Tunable by Alloy Composition. *J. Am. Chem. Soc.* **133,** 6711–6719 (2011).

46. Wells, A. F. *Structural inorganic chemistry*. (Clarendon Press ; Oxford University Press, 1984).

47. Shannon, R. D. Revised effective ionic radii and systematic studies of interatomic distances in halides and chalcogenides. *Acta Cryst A, Acta Cryst Sect A, Acta Crystallogr A, Acta Crystallogr Sect A, Acta Crystallogr A Cryst Phys Diffr Theor Gen Crystallogr, Acta Crystallogr Sect A Cryst Phys Diffr Theor Gen Crystallogr* **32,** 751–767 (1976).

48. Hegde, M., Wang, T., Miskovic, Z. L. & Radovanovic, P. V. Origin of size-dependent photoluminescence decay dynamics in colloidal γ-Ga2O3 nanocrystals. *Applied Physics Letters* **100,** 141903 (2012).

49. Wang, T. & Radovanovic, P. V. In situ enhancement of the blue photoluminescence of colloidal Ga2O3 nanocrystals by promotion of defect formation in reducing conditions. *Chem. Commun.* **47,** 7161–7163 (2011).

50. Yu, Q., He, H., Gan, L. & Ye, Z. The defect nature of photoluminescence from a porous silicon nanowire array. *RSC Advances* **5,** 80526–80529 (2015).

51. Sillen, A. & Engelborghs, Y. The Correct Use of 'Average' Fluorescence Parameters. *Photochemistry and Photobiology* **67,** 475–486 (1998).

52. Niki, E. Action of ascorbic acid as a scavenger of active and stable oxygen radicals. *Am. J. Clin. Nutr.* **54,** 1119S–1124S (1991).

53. Som, S., Raha, C. & Chatterjee, I. B. Ascorbic acid: a scavenger of superoxide radical. *Acta Vitaminol. Enzymol.* **5,** 243–250 (1983).

54. Adamek, E., Baran, W. & Sobczak, A. Effect of FeCl3 on the photocatalytic processes initiated by UVa and vis light in the presence of TiO2–P25. *Applied Catalysis B: Environmental* **172–173,** 136–144 (2015).

55. Georgaki, I., Vasilaki, E. & Katsarakis, N. A Study on the Degradation of Carbamazepine and Ibuprofen by TiO2 & ZnO Photocatalysis upon UV/Visible-Light Irradiation. *American Journal of Analytical Chemistry* **05,** 518–534 (2014).

56. Ökte, A. N., Resat, M. S. & Inel, Y. Influence of hydrogen peroxide and methanol on the photocatalytic degradation of 1,3-dihydroxybenzene. *Toxicological & Environmental Chemistry* **79,** 171–178 (2001).

57. Shen, M. & Henderson, M. A. Identification of the Active Species in Photochemical Hole Scavenging Reactions of Methanol on $TiO_2$. *The Journal of Physical Chemistry Letters* **2,** 2707–2710 (2011).

58. Anpo, M. & Kamat, P. V. *Environmentally Benign Photocatalysts: Applications of Titanium Oxide-based Materials*. (Springer Science & Business Media, 2010).

59. Phani, A. R. *et al.* Preparation and characterization of bulk ZnGa2O4. *Journal of Materials Science* **33,** 3969–3973 (1998).

60. Liu, Q. *et al.* Single-Crystalline, Ultrathin ZnGa2O4 Nanosheet Scaffolds To Promote Photocatalytic Activity in CO2 Reduction into Methane. *ACS Appl. Mater. Interfaces* **6,** 2356–2361 (2014).

61. Errandonea, D., Kumar, R. S., Manjón, F. J., Ursaki, V. V. & Rusu, E. V. Post-spinel transformations and equation of state in ZnGa2O4: Determination at high pressure by in situ x-ray diffraction. *Phys. Rev. B* **79,** 024103 (2009).

62. Saharudin, K. A., Sreekantan, S. & Lai, C. W. Fabrication and photocatalysis of nanotubular C-doped TiO2 arrays: Impact of annealing atmosphere on the degradation efficiency of methyl orange. *Materials Science in Semiconductor Processing* **20,** 1–6 (2014).

# Appendix

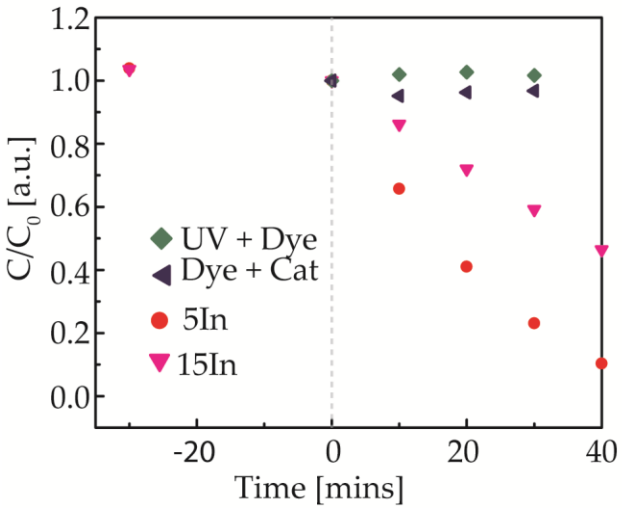


**Figure A1: Relative degradation of Rh-590 for control experiments. Green diamond show dye exposed to UV without a catalyst present. Blue triangles represent dye in presence of catalyst (15%In) with no UV exposure. Red circles and pink triangle on the graph are representative samples with catalyst, dye, and UV exposure. Dashed grey line represent when the catalyst has been added for those experiments that require a catalyst.**

**Table A1: Summary for $Ga_{2-x}In_xO_3$ synthesized at 300 °C**

| Nominal Percentage Indium [%] | Surface Area [$m^2/g$] | $K_{app}$ [$min^{-1}$] |
|---|---|---|
| 5 | 238.1 | 0.052 ± 0.009 |
| 10 | 235.8 | 0.027 ± 0.014 |
| 15 | 209.6 | 0.047 ± 0.004 |